Nano- and Micro-geochronology in Precambrian Zircons by Atom-Probe Tomography and SIMS: New Tools for Old Minerals

John W. Valley¹, David A. Reinhard², Aaron J. Cavosie^{1,3}, Takayuki Ushikubo^{1,4}, Daniel F. Lawrence², David J. Larson², Thomas F. Kelly², David Snoeyenbos⁵, Ariel Strickland¹

June 4, 2014

To be submitted to American Mineralogist

(invited by Chief Editor Keith Putirka)

¹Department of Geoscience, University of Wisconsin, Madison, WI 53706, USA

²CAMECA Instruments, Madison, WI 53711, USA

³Department of Geology, University of Puerto Rico, Mayaguez, PR 00681, USA

⁴Current address: JAMSTEK, Kochi Institute for Core Sample Research, Nankoku City, Japan

⁵Box 513, Chesterfield, MA 01012, USA

Abstract

Atom-probe tomography (APT) and secondary ion mass spectrometry (SIMS) provide complementary *in situ* element and isotope data in minerals such as zircon. SIMS measures isotope ratios and trace elements from 1-20 µm spots with excellent accuracy and precision. APT can identify mass and 3-D position of individual atoms (±0.3 nm) in 100-nm-scale samples, volumes one million times smaller than SIMS. APT data provide unique information for understanding crystallization, thermal history and mechanisms of mineral reaction and exchange. This atomistic view for zircon enables evaluation of the fidelity of geochemical data because it:

a) provides new understanding of radiation damage, and b) can test for intracrystalline element mobility. Nano-geochronology is one application of APT in which Pb isotope ratios from subµm domains of zircon can provide model ages of small crystals or identify later magmatic and metamorphic reheating.

Following SIMS analysis, eleven needle-shaped specimens \sim 100nm in diameter were sampled from three Archean and Hadean zircons by focused ion beam milling and analyzed with APT. The 3-D distribution of Pb and other incompatible elements (Y, REEs) differs at the atomic scale. Zircon JH4.0 (4.007 Ga, 01JH13b/2.5M/8-4, Jack Hills, W. Australia) is homogeneous in Pb, Y and REEs. In contrast, Pb and YREEs are clustered in sub-equant 5-10 nm diameter domains, spaced <50 nm apart in zircons ARG2.5 (2.542 Ga, ARG05-28-2, Grouse Creek Mts., Utah) and JH4.4 (4.374 Ga, 01JH36-69, Jack Hills). U and Th are not co-localized with Pb in clusters and appear to be homogeneously distributed in all three zircons. The analyzed domains suffered from 4 to 8 x 10^{15} α -decay events/mg due to U and Th decay and yet all zircons yield U-Pb ages by SIMS that are better than 97% concordant, consistent with annealing of radiation damage. The 207 Pb/ 206 Pb ratios for the 100-nm-scale specimens measured by APT average 0.17 for ARG2.5, 0.42 for the JH4.0 and 0.52 for JH4.4. These ratios are less precise (\pm 10-18% 2σ) due to the ultra-small sample size, but in excellent agreement with values measured by SIMS

(0.1684, 0.4269, and 0.5472, respectively) and the crystallization ages of the zircons. Thus Pb in these clusters is radiogenic, but unsupported at nm-scale by parent isotopes. For the domain outside of clusters in JH4.4, the ²⁰⁷Pb/²⁰⁶Pb ratio is 0.3, consistent with the SIMS value of 0.2867 for the zircon overgrowth and an age of 3.4 Ga. In ARG2.5, all Pb is found concentrated in clusters and there is no detectable Pb remaining outside of the clusters. The Pb-Y-REE-rich clusters and lack of correlation with U in ARG2.5 and JH4.4 are best explained by diffusion of Pb and other incompatible elements into 5-10 nm amorphous domains formed by α -recoil. Diffusion distances of ~20 nm for these elements in crystalline zircon are consistent with heating at temperatures of ~800°C for ~2m.y. Late reheating events are identified and dated by APT from ²⁰⁷Pb/²⁰⁶Pb model ages in clusters in JH4.4 and by the absence of detectable Pb outside of clusters in ARG2.5. SIMS dates for the rims independently confirm reheating of ARG2.5 and JH4.4, which were xenocrysts in younger magmas when rims formed. It is proposed that most domains damaged by α-recoil were annealed at ambient temperatures above 200-300°C and only a small number were amorphous and available to concentrate Pb at the time of reheating. The clusters in JH4.4 document Pb mobility at the sub-50-nm scale, but show that µm-scale domains analyzed by SIMS were closed systems. Thus, the reliability of other geochemical analyses of zircon, including oxygen isotope ratios, can be evaluated by these means. These results verify the age of this zircon and support previous proposals that differentiated crust existed as early as 4.4 Ga and that the surface of Earth was relatively cool and habitable before 4.3 Ga. The absence of enriched clusters in JH4.0 shows that this zircon was not reheated during crustal recycling. Thus APT data provide information about crustal reworking even for zircons where no overgrowth is recognized.

Introduction

Atom Probe Tomography (APT) is an analytical tool that has only recently become available for studies of electrically insulating phases including silicate minerals. In terms of spatial resolution and detection limits for chemical analysis, the capabilities are intermediate between Secondary Ion Mass Spectrometry (SIMS) and Transmission Electron Microscopy (TEM) (Fig. 1, Gault et al. 2012). Similar to TEM, sample sizes are at the 100-nm-scale and individual atoms are routinely located in 3-D. Like SIMS, atoms can be identified and isotope ratios measured. No other technique provides spatially resolved mass spectrometry and 3-D mapping at single-atom scale. The complementary application of APT and SIMS to zircons offers unique opportunities to assess sample heterogeneity, radiation damage, and element mobility, issues that U-Pb geochronologists have wrestled with for 100 years.

Less than 20 years after the discovery of radioactivity, Holmes (1913) estimated the age of the Earth based on decay of U to Pb. Although limited by the technology and understanding of his day, this pioneering work laid the foundations for modern geochronology and identified many critical aspects including the retentiveness of zircon, the closed-system criteria, and possible Pb mobility. Geochronology has progressed greatly since Holmes' first studies (Condon and Schmitz 2013), but radiation damage and Pb mobility in zircon remain poorly understood at the atomic scale.

The effects of radiation damage on bulk properties of zircon are well-known and include increases in volume, water content, and dissolution rate; and decreases in birefringence, elastic moduli, and hardness (Ewing et al. 2003). In extreme cases, metamict zircon is fully altered to a glass-like material. The degree of radiation damage also strongly influences diffusion and exchange rates, and thus the fidelity of zircon geochemistry. The very property that makes zircons prized for geochronology is also its Achilles' heel.

There are many causes of radiation damage including fission tracks, β -tracks, α -tracks, and α -recoil. The later, recoil of a newly formed daughter atom upon emission of a α -particle is the dominant cause of damage to the zircon crystal structure. All natural zircons have some degree of radiation damage and the gradations of damage can be described by percolation theory (Salje et al. 1999; Ewing et al. 2003). For low doses of radiation, the damaged domains are isolated. In this state, the grain is said to be below the first percolation point and crystalline zircon surrounds damaged volumes armoring them from exchange. The first percolation point (\sim 2 x10¹⁵ α -decays/mg, Rios et al. 2000) represents the condition where damaged domains overlap to form continuous pathways throughout the crystal or volume of interest. At this point, amorphous domains constitute 30-40% by volume and rates of dissolution and exchange are enhanced in comparison to volume diffusion, which is slow in crystalline zircon.

The increasing use of *in situ* spot analysis for sub-domains of a zircon reinforces the importance of evaluating localized radiation damage, which can facilitate elemental and isotopic exchange and erroneous results for measurements of U-Pb age (Ewing et al. 2003; Cavosie et al. 2004; White and Ireland 2012); oxygen isotope ratios (Valley et al. 1994; Valley 2003; Cavosie et al. 2005; Booth et al. 2005; Gao et al. 2014; Wang et al. 2014) and trace elements (Hoskin and Schalteggar 2003; Cavosie et al. 2006). Just as the concentrations of U and Th can vary greatly within a crystal, altered radiation-damaged domains can be localized and intergrown with pristine crystalline zircon at a sub-grain scale (Chakoumakis et al. 1987).

Geochemists have employed a wide range of procedures to evaluate radiation damage and the fidelity of their zircon data. For bulk multi-grain samples, low magnetism zircons typically contain less U, Th and REEs, and have less damage. Low magnetism zircons yield more concordant ages (Silver 1963; Silver and Deutsch 1963; Krogh 1982) and primary values of δ^{18} O (Valley et al. 1994; Valley 2003). Likewise, soaking in HF removes metamict zircon from a mineral concentrate, which improves oxygen isotope data (King et al. 1998), but can leach Pb

from damaged domains. The chemical abrasion method for U-Pb analysis employs high temperature annealing followed by a series of partial dissolution steps to remove progressively less damaged material (Mattinson 2005). For *in situ* studies of polished surfaces in zircon. domains of questionable reliability can be identified by a range of imaging techniques including: optical examination for micro cracks, porous zircon, anomalous inclusions or reduced birefringence; cathodoluminescence imaging (CL), back-scattered electron imaging (BSE), and electron back-scatter diffraction (EBSD) in a scanning electron microscope (SEM); laser Raman spectroscopy; and fuming with HF (Krogh and Davis 1975; Pidgeon 1992; Corfu et al. 2003; Nasdala et al. 2003; Reddy et al. 2006). Radiation damage can also be imaged by HR-TEM (Ewing et al. 2003; Utsunomiya et al. 2004, 2007). Likewise, SIMS analysis spots can identify pristine domains that yield concordant ages and low concentrations of non-formula elements such as Ca and Fe (Geisler and Schleicher 2000; Rayner et al. 2005; Cavosie et al. 2005; Geisler et al. 2007; Bouvier et al. 2012), and multiple analyses for different isotope systems can be correlated with zoning patterns (Cavosie et al. 2006). One promising new approach is to monitor the molecular ion, ¹⁶O¹H, during SIMS analysis of ¹⁸O/¹⁶O as a guide to water content, and which may correlate to radiation damage (Pidgeon et al. 2013; Wang et al. in review). It is always a good idea to look at zircons carefully by a range of techniques before analysis, however the above procedures provide only an indirect measurement of properties that can correlate with alteration. No previous study has chemically analyzed alteration at an atomic scale.

The interpretation of dates and other data for Archean and Hadean zircons requires special attention to radiation damage. Even zircons with low [U] and [Th], below a few 100's of ppm, experience enough α -decay to exceed the first percolation point if not annealed. Fortunately, in many zircons radiation damage has been partially healed and primary compositions of the zircon are reliably preserved. Uncertainty about post-crystallization modification has fueled controversy regarding the ages and the fidelity of geochemistry, especially for Hadean zircons (Nelson et al.

2000; Parish and Noble 2003; Whitehouse and Kamber 2002; Hoskin 2005; Nemchin et al. 2006; Holden et al. 2009; Kusiak et al. 2013a, b). Hadean zircons exist only as detrital grains or xenocrysts and are the oldest samples from the early Earth. Determination of their origins is critically dependent on analysis of primary magmatic composition.

In this study, we used a variety of imaging and microanalysis protocols by SEM and SIMS to select three Archean and Hadean zircons for APT. The combination of APT and SIMS provides an unprecedented record of the atom-scale distribution of isotopes and mobility of trace elements, including Pb, within the zircons. These techniques allow direct measurement of the effects of radiation damage and establish criteria for distinguishing pristine vs. disturbed zircon compositions. In addition, the timing of crystallization and cryptic reheating events, measurable by no other method, is assessed for sub-um samples of zircon.

Techniques

SIMS- Secondary Ion Mass Spectrometry

The three zircons of this study were analyzed in multiple sessions at five different labs to determine the age, stable isotope ratios and trace element composition. JH4.4 was dated by SHRIMP-II at the Chinese Academy of Geological Sciences, Beijing (Cavosie et al. 2004) and at Curtin University (Cavosie et al. 2007). JH4.0 was dated at Curtin University (Cavosie, 2005). ARG2.5 was dated by SHRIMP-RG at the Stanford/ USGS Micro-Analysis Center (Strickland et al. 2011a). SHRIMP-II methodology is described previously (Williams et al. 1998; Cavosie et al. 2004). Age determinations involved 7 measurement cycles for each mass, and were calibrated using the zircon U-Pb standard, CZ3 (Pidgeon et al. 1994). Grains of CZ3 were located within the same epoxy mount as the sample. Multiple analyses of CZ3 were made, using a 'bracketing strategy', whereby standard analyses were before, during, and after sample analyses. Data were reduced using the program Squid (Ludwig 2001a); sample analyses were corrected for common

Pb using measured 204 Pb. The 2σ uncertainty in the mean of the Pb/U ratio for the standard analyses was 0.55% for JH4.4. Graphical representations of the U-Pb data were prepared using the program Isoplot (Ludwig 2001b).

Oxygen isotope ratios were measured by IMS-1270 at the University of Edinburgh (δ^{18} O, Cavosie et al. 2005) and by IMS-1280 at WiscSIMS, UW-Madison (δ^{18} O, δ^{17} O, Valley et al. 2007, 2014a; Ushikubo et al. 2008; Kita et al. 2009; Valley and Kita 2009). Trace elements were measured by IMS-4f in Edinburgh (Cavosie et al. 2006) and IMS-1280 at WiscSIMS (this study). Measurements at WiscSIMS also include trace elements, [Li] and δ^7 Li (Ushikubo et al. 2008; Bouvier et al. 2012). The analytical techniques of each analysis are reported in these papers.

A total of 25 trace elements were analyzed in situ by SIMS (Table 3) using procedures described elsewhere: Li, Al, P, Ca, Ti, V, Fe, Y, La, Ce, Pr, Nd, Sm, Eu, Gd, Tb, Dy, Ho, Er, Tm, Yb, Lu, Hf, Th, and U (Page et al. 2007; Fu et al. 2008; Ushikubo et al. 2008).

APT- Atom Probe Tomography

Atom Probe Tomography was conducted using a LEAP 4000X HR® at the CAMECA Atom Probe Technology Center, Madison, Wisconsin. Zircon slices measuring approximately 3 x 5 x 30 μ m were removed from polished faces of each crystal and milled to make multiple needle-shaped specimens using a focused ion beam (FIB) guided by cathodoluminescence (CL) and field-emission SEM (Figs. 2 a-d). Six specimens are potentially obtained from each FIB lift-out with final dimensions of ~100 nm at the specimen tip and analyzable lengths of 500-1500 nm (Figs. 2c, d). The orientation of each needle is normal to, and pointing towards, the polished surface.

The local-electrode atom probe (LEAP) instrument is described in detail elsewhere (Larson et al. 2013; Kelly and Larson 2012; Gault et al. 2012). Analysis capabilities and protocols differ for electrically conducting vs. insulating materials. Analysis of insulators has recently become

practical by development of commercial laser-stimulated ionization (Kellogg and Tsong 1980; Gault et al. 2006; Bunton et al. 2007). Insulating specimens are cooled to 50K at high vacuum and a high voltage (typically 4-14 kV) is applied (Fig. 3a). In this study, a pulsed UV laser (355 nm wavelength, pulse energy 400 pJ, 200 kHz repetition rate) was focused on the specimen to a 2.5 µm diameter, 4-sigma spot to promote field evaporation of, on average, approximately 0.008 ions/pulse. Ions travel through vacuum toward a time-of-flight measurement that is used to determine the isotopic identity. The LEAP 4000X HR incorporates a curved reflectron compensator (Panayi patent, 2012) (Fig. 3b), which improves the mass resolving power to about 1200 (M/ΔM, FWHM) at the ²⁸Si⁺ peak while retaining the field of view of about 150 nm. For the specimens used in this study (~100 nm diameter at tip, radius of curvature < 100 nm), the spatial resolution of detected atoms is about ± 0.3 nm in X-Y-Z coordinates. From 10^7 to 4×10^8 ions were detected per specimen at rates of $\sim 10^7$ ions/hour. In principle, all ions are detected with an equal efficiency of ~37%. The ion detection efficiency is determined by the 60% detection efficiency of the microchannel plates times the 80% transmission of the mesh on both entrance and exit. The minimum detection limit is ~ 10 ppma (parts per million of atoms per peak) for these data, but the limited volume of the analysis, and in some cases molecular interferences, can limit detection. Spectra must be individually evaluated as some elements form ionized molecules, and some peaks have isobaric interferences.

Composition Determinations

Composition values are determined in atom probe tomography as follows. For microchannel plate detectors, the ion detection probability is known to be uniform with mass up about 500 Da so all ions are assumed to have the same detection probability. A range is defined in the mass spectrum to denote the start and end of a given peak. The counts within this range are defined as the raw counts. The background counts are determined by examining the nominal

level of the spectrum on either side of the range and estimating the background contribution in the range by interpolation. The net signal counts are thus raw counts minus background counts. The composition of any volume in the 3D image is determined simply as the sum of all the atoms in that volume.

Identification of peaks in the mass spectrum is straightforward when the peaks are isolated, though a multiplicity of peaks can be generated for an element. Each of the possible charge states (n=1, 2, 3, ...) is considered for any given isotope. Molecular ions do occur in field evaporation and they can be compositions that are altered by the presence of the high electric fields on the specimen (e.g., H₃O⁺ is a common ion). Hydrides of almost any element can form which complicates analyses for some specimens as discussed below.

When peak overlaps occur, a peak decomposition approach is used in the IVAS software (Integrated Visualization and Analysis System, Kunicki et al. 2006). For a mass spectrum for any given subvolume, this approach computes the probability that the peak may have contributions from neighboring peaks. For stable isotopes, this probability is based on average terrestrial isotope ratios. These ratios do not apply to radiogenic isotopes such as Pb. In this latter case, we relied on their mass position, the concentrations of parent isotopes, and reasonable ages. For instance, as will be shown, the fact that there is no Pb found in the matrix of ARG2.5, there is a physically sensible amount of Pb (and ²⁰⁷Pb/²⁰⁶Pb ratio) in the matrix of JH4.4 and there is a lot of Pb in the clusters of both, leads to a self-consistent interpretation that quantitatively matches the SIMS results.

In computing the compositions, we used a built-in function in IVAS to quantify the local background next to each peak and then subtract this background for the net signal. It is not possible to correct for background in the ion maps or tomography as each datum may be signal or background. Any single count is indeterminate as to whether it is a signal or background count. Only in collective measurements such as composition determinations from a volume can the

background be subtracted. One can take the ratio of signal to background for some peak and note that statistically, any given datum will have this probability of being a signal event.

The sources of background events are manifold: a) residual gas in the vacuum chamber can adsorb on the specimen and become a field ion, b) evaporation of ions between pulses will not be timed correctly and they contribute to the background continuum, c) electronic noise in the detector, d) dissociation of a molecular ion during acceleration into one charged and one uncharged entity can lead to untimed events, and even e) cosmic rays may excite the detector. Most of these sources of background are low as evidenced by atom probe's high signal-to-noise ratio in general. When running a new type of material, the run conditions are first established for any specimen to minimize any out-of-time evaporation. This work is done before any data are quantified.

For any type of specimen, background levels may be optimized by using a high pulse rate, lower temperature, high detection rate, high pulse fraction (voltage pulse mode only), proper laser pulse setup (focus, spot size, alignment of laser), proper laser pulse energy (not too high, not too low, see Larson et al. 2013 p. 90), and specimen surface (shape, absorbance of laser energy, thermal diffusivity, band gap; see table 4.1 of Larson et al. 2013).

The uncertainty in the composition determination is computed from the square root of the sum of raw plus background counts. The range for peak integration and settings for background measurement are set visually from an expanded view of the spectrum. Since the binning-induced peak size has an error uncertainty, the measurement is performed five times and the errors are added in quadrature.

The detection sensitivity of the APT technique (Larson et al. 2013, p. 166) can be assessed from the number of background counts in a range. Using the definitions of Currie (1968) for detectability, the net counts of a peak of interest that must be present in the spectrum in order to avoid being obscured by the background can be calculated from 4.65 times the square

root of the background. If the net counts are greater than that number we expect to see the peak above the background level 95% of the time. The detection limit for any particular isotope is thus diminished if the corresponding peak resides on the tail of another peak. Clustering of low concentration elements improves the detectability if the clusters can be isolated as is the case in this work.

Constructing the 3D Image

Constructing a 3D image from the raw data requires converting an X,Y hit position on the detector to an x,y,z position of the atom in real space within the sample. For a review of atom probe reconstruction procedures, see Larson et al. (2013). Detector hits are first back projected onto a curved surface that represents the specimen surface. The sequence of hits on the detector is the sequence in which the atoms are back projected and this constitutes the third dimension of an image. A projection law must be used to back project the atom. The projection law is determined by the shape of the specimen apex, but it is not perfectly known in today's instruments. To first order, the needle-shaped specimen can be modeled as a cone with a spherical endcap for which a projection can be modeled analytically. Note however, that though the relative position of atoms may be determined by this procedure, absolute positioning, i.e., accurate spatial scaling, is not achieved without additional information. A physical parameter such as atomic density or the specimen apex radius is used to fix the scaling. Furthermore, because the specimen does not possess a perfect spherical endform, the reconstruction will contain errors whose local magnitude depends on the local deviation of the endcap from a spherical geometry.

In amorphous materials, the endcap can be smooth and approximately spherical though not tangential to the cone. In this case, the spherical approximation, with accounting for a nontangential cap on cone, is good. For single-phase crystalline materials, low-index poles usually form small facets on the surface because atoms will not evaporate from the middle of a close-packed plane, but rather, the atoms on the edges of planes evaporate and the plane shrinks from its edges. These facets cause local deviations from a spherical surface and ion trajectories are splayed outward from the center of poles as a result. Spatial resolution in metals between poles has been shown to be better than 150 pm (Kelly et al. 2009). Thus, though very high spatial resolution is achieved in most images, it is not necessarily achieved in all locations of the image. Minerals generally do not show this tendency to form obvious facets, which means that the spatial resolution should be more uniform throughout the image.

In multiphase specimens, the surface can develop topography due to differences in the evaporation fields of the different phases. That is, if a small phase requires a high electric field to evaporate relative to its surrounding matrix, then it will tend to protrude further into the high electric field region before evaporating. Thus differential evaporation leads to a protrusion of the high-field material, which alters the trajectories of the ions toward the detector. The simple spherical-projection reconstructions that are prevalent today do not account for these protrusions and the spatial resolution locally can be several nm for a large evaporation field difference and a large size of the second phase. In the limit of a very small second phase (e.g., a 10-nm cluster) or a very small evaporation field difference, this trajectory aberration disappears.

Methods for identifying clusters in atom probe data have been the subject of a variety of approaches (Blavette et al. 1988, Vurpillot et al. 2004, De Geuser et al. 2006, Hyde and Marquis 2009, Stephenson et al. 2011). The details of these approaches are beyond the scope of this paper. Essentially, the local environment of any given solute atom in a dataset is assessed for the presence of other solute atoms based on a) spatial proximity or b) local composition. In a), geometric rules have been developed to associate atoms with a cluster if they are within a certain small distance of any other solute atom in the cluster and in b) if the local composition exceeds a value that would obtain were the atom distributions random. Alternatively, since the local

composition can be computed at any point in the 3D image, isoconcentration surfaces can be contoured through the data. These surfaces will surround volumes of high solute content in the case of small precipitates or clusters. In IVAS, such isoconcentration surfaces can be modified in real time using a composition slider bar to adjust the value of composition for the dividing surface. Given the nature of the clusters in this paper, we have found this latter approach to give the most straightforward interpretation of the clusters. For the purposes of composition determination inside the clusters, we have used 3-at.% Y as the defining surface in JH4.4 and 0.5-at.% Y in ARG2.5. In order to extract the clusters from the 3D volume and calculate the composition of surrounding zircon in JH4.4, we have used 1-at.% Y as the defining surface. This approach excludes a small zone at the cluster surface but it minimizes the variability of the compositions. Geometric cluster analyses were also performed in IVAS (Maximum Separation Method) and they yielded different answers for the number of clusters. The result is therefore subjective. We avoided obvious errors from these analyses: it was not acceptable to have connective volumes between clusters and it was not acceptable to break up obvious clusters. However, the number of clusters cited in this paper is the midpoint of these geometric cluster analyses. We estimate that the cluster number density is correct to within a factor of 2.

The mass resolving power (MRP) in time-of-flight spectroscopy depends on the ion flight time since $MRP=m/\Delta m=t/\Delta t$ (m= mass, t= time of flight, and $\Delta t=$ time of departure spread) Δt should be independent of flight time for laser pulsing. For this reason, the mass at which the MRP is measured should be stated. It is preferred to cite MRP values measured at mass/charge (m/n) ~30. In this work, there is a strong peak at m/n=32 which corresponds to $^{16}O_2^+$. The MRP valued measured on this peak ranged between 900 and 1100 (FWHM) for all of this work.

Non-metamict zircon is a well-behaved material in an atom probe. It has high values of thermal diffusivity, which leads to greater cooling rates and therefore better mass-resolving power in laser pulsing. It can withstand high hydrostatic stress (the stress in the specimen varies

as the square of electric field which is very high). The fact that zircon runs well is a sign that it has a high strength relative to its average evaporation field.

Molecular Species in APT Spectra

Molecular species are common in atom probe spectra, which can lead to sample-specific artifacts. Failure to identify such species can lead to erroneous concentrations. For instance, hydride interferences are common and can cause elevated counts for peaks at mass, m+1, (and corresponding diminished peak counts at m). This is especially problematic for measurement of isotope ratios if the higher mass peak at m+1 is at lower abundance, as is the case for the commonly analyzed stable isotope ratios of H, C, N, O, Mg, Si, Cl, S, Ca, and Cr. Heck et al. (2014) report special care in measuring carbon isotope ratios from pre-solar nanodiamonds, which show an unexplained instrumental bias and anomalously high measured levels of ¹³C that may result from an isobaric interference on ¹³C or deadtime corrections for ¹²C. The hydride interference at 13 Da is especially challenging in nanodiamonds because ¹³C/¹²C ratios average 0.015 and significant amounts of H can reside in the specimen on the unavoidable grain boundaries.

Zircon is nominally anhydrous when fully crystalline, however water content typically increases with radiation damage and can exceed 10 wt% in metamict zircons (Aines and Rossman, 1986; Nasdala et al. 2001a, 2003; Geisler et al., 2003; Utsunomiya et al., 2007). In this study, predominantly crystalline domains of zircon were selected based on CL zoning, concordant U-Pb ages, and REE patters, and verified by EBSD in the case of grain JH4.4. The current protocol for oxygen 2-isotope analysis at WiscSIMS is to tune mass 17 to 16 OH, which provides a monitor of H in each spot analyzed (Wang et al. 2014). However, this procedure was not yet developed when δ^{18} O was analyzed in these zircons. Hydride interferences are evaluated for several adjacent peak positions in the APT spectra and their importance is found to be highly

variable according to the element and proportions involved. The intensity of hydride interferences is significantly reduced for doubly ionized species (Tsong et al. 1983, Heck et al. 2014) and thus for this study, it is unlikely that the intensity of (²⁰⁶PbH)⁺⁺ interference on ²⁰⁷Pb⁺⁺ is significant for the range of ²⁰⁷Pb/²⁰⁶Pb ratios measured (0.17 to 1.2) and the analytical precision reported (±3-7%).

Hydrogen is readily detected in an atom probe and all spectra have prominent H peaks at 1-3 Da (Fig. 4). A key question is what is the origin of the hydrogen? The detected hydrogen may come from the vacuum chamber volume, from the specimen itself, or both. Because hydrogen is difficult to pump, it is always a major component of the residual gas in an ultra-high vacuum system. The level of residual hydrogen can depend on previous samples, the length of time since venting, and the general system vacuum. If hydrogen mapping and quantification are to be performed in an atom probe, a careful effort must be made to distinguish its source. Hydrogen may appear as a monatomic ion (H⁺), as a molecular ion (H₂⁺), or as a hydride of other elements in the material.

We tested the hydride interference for single ionizations and adjacent oxygen peaks at 16-18 Da (Fig. 5b). The apparent values of δ^{18} O mostly range from 100 to 400% higher than the true value for each zircon. The largest discrepancies are seen for the specimens with the highest ${}^{1}\text{H}/{}^{16}\text{O}$ ratios. These differences are interpreted to result from isobaric interferences at 18 Da from ${}^{1}\text{H}_{2}{}^{16}\text{O}$, ${}^{17}\text{OH}$, and ${}^{16}\text{O}{}^{2}\text{H}$. These isobars are cleanly separated from the ${}^{18}\text{O}$ peak at MRP = 2500 by SIMS (Valley and Graham 1991 see Fig. 2; Kita et al. 2009), however the hydrides are not resolved at MRP = 1000 by APT causing elevated ratios of the 18 Da/16 Da peaks (Fig. 5b). The hydride interference of ${}^{1}\text{H}^{16}\text{O}$ on ${}^{17}\text{O}$ can only be resolved by SIMS at MRP = 5000 (Kita et al. 2009) and the effect for measurements by APT is very large due to the low concentration of ${}^{17}\text{O}$. Thus SIMS is preferred over APT for accurate analysis of oxygen isotope ratios at natural abundance levels.

Pb Isotope Ratios by APT

The APT spectra for each zircon shows peaks for doubly ionized ²⁰⁶Pb²⁺, ²⁰⁷Pb²⁺, and ²⁰⁸Pb²⁺ at mass/charge = 103, 103.5, and 104 Da, respectively (Fig. 6). No singly ionized Pb⁺ is detected at 204-208 Da. The non-radiogenic isotope, ²⁰⁴Pb, was not detected, consistent with SIMS data that show low 204 Pb/ 206 Pb (< 1 x10⁻⁴, < 9 x 10⁻⁵, and < 6 x10⁻⁶ for JH4.4, JH4.0 and ARG2.5, respectively). There are no apparent interferences for peaks at 103 and 103.5 Da (²⁰⁶Pb and ²⁰⁷Pb). A small contribution of ¹H²⁰⁶Pb for ²⁰⁷Pb can't be ruled out, but as discussed above under Molecular Species it is less than reported uncertainty and unlikely to be as large as 1% of the ²⁰⁷Pb peak. The peak for ²⁰⁸Pb²⁺ at 104 Da, however, suffers from an isobaric interference by $(^{28}\text{Si}_2^{16}\text{O}_3)^+$ that cannot be resolved at MRP = 1000. The identification of this peak is verified for ARG2.5 (Fig. 6) where all of the detectable Pb is in clusters. For atoms located within the clusters, there are three Pb peaks, but the peak at 104 is disproportionately high compared to SIMS data that show $^{208}\text{Pb}/^{206}\text{Pb} = 0.095$, indicating that much of the 104 Da peak is not from ²⁰⁸Pb (Fig. 6a). Outside of clusters, there are no detectable peaks at 103 and 103.5 Da showing that there is no Pb and thus the peak at 104 Da is Pb-free (Fig. 6b). The series of peaks seen for Si, SiO, and SiO₂, suggest that Si₂O₃ will be present at 104 Da and this is confirmed by the small peak at 105 Da in Figure 6b, which is ~5% as intense as 104, consistent with singly substituted ²⁹Si or ¹⁷O in Si₂O₃ (natural abundances are: 29 Si/²⁸Si ~0.050 and 17 O/¹⁶O ~ 0.00038). The small peak at 105 Da further indicates that hydrides were not significant in this sample. A significant interference from (Si₂O₃H)⁺ would dominate the 105 Da peak, which is not seen. Thus for all of the zircons in this study, ratios of ²⁰⁷Pb/²⁰⁶Pb can be measured either for entire specimens or for sub-domains such as clusters. The concentration of ²⁰⁸Pb can't be deconvoluted from its interference in zircon, but this might be possible in Si-free minerals such as baddeleyite or phosphates (Snoeyenbos et al. 2012).

Samples

Three zircons were selected for study by APT based on earlier SEM and SIMS studies. The analyzed domains range in age from 4.4 to 2.5 Ga. The sample numbers of these three zircons have been simplified from those reported in earlier papers to designate locality and age. The abbreviated and full names are: JH4.4 = 01JH36-69, JH4.0 = 01JH13b/2.5M/8-4, and ARG2.5 = ARG05-28-2. The oldest zircon, JH4.4, has been examined in the most detail and provides the best comparison of data from SIMS and APT. The other two samples illustrate similarities and differences, and provide additional support for interpretations of the APT results.

JH4.4

JH4.4 is a detrital zircon (01JH36-69), recovered by electric pulse disaggregation of quartzite (sample 01JH36) from the Jack Hills, which are in the Narryer belt of the Yilgarn craton, Western Australia. The locality is midway between the East and West Traverses of Cavosie et al. (2004) and is ~1 km NE of Eranandoo Hill on the West Traverse where the first 4.3 Ga (Compston and Pidgeon 1986) and 4.4 Ga (Wilde et al. 2001) zircons from Earth were found. This quartzite rock is a metamorphosed sandstone as evidenced by dark bands of detrital minerals, dominantly chromite and zircon (minor rutile), that outline flattened cross beds (Fig. 7a). The rock also contains minor metamorphic chromian-muscovite, tourmaline and monazite. Whole-rock analysis by XRF shows 96.9 wt% SiO₂; minor Al and K in white mica; Cr in both mica and chromite; and 87 ppmw Zr as detrital zircon (Cavosie et al. 2004).

Because of its large size (230 x230 x430 µm) and old age (4.4 Ga, Cavosie et al. 2007; Valley et al. 2014a), zircon JH4.4 was ground and re-polished 4 times. The first two surfaces were ground shallowly so as not to remove smaller zircons in the same mount. As a result, surfaces #1 and #2 (Cavosie et al. 2004, 2005, 2006) did not penetrate the core of the crystal, and only exposed subsequent levels of the wide younger overgrowth; CL images of surfaces 1 and 2

showing analysis spots and patchy CL patterns are published in those papers. Eleven SIMS analyses of age were made on surface 1 with the oldest spot in the core yielding 85% concordance and a $^{207}\text{Pb}/^{206}\text{Pb}$ age of 4324 ±18 Ma (Cavosie et al. 2004). One analysis of the overgrowth at the crystal termination yielded discordance (50%) and ~3.4 Ga. Surface 2 was analyzed for $\delta^{18}\text{O}$ five times, but only one pit ($\delta^{18}\text{O} = 4.6\%$) in the core was interpreted as normal in appearance by SEM; others were rejected as irregular by criteria described by Cavosie et al. (2005). The rejected values average 4.6% in the core and 6.2% in the rim. REEs were measured twice on surface 2 (Table 3, Cavosie et al. 2006).

JH4.4 was subsequently deeply ground to approximately its mid-section and repolished, sequentially exposing surfaces #3 and #4 that were less than a few µm apart. These surfaces were imaged by SEM (CL, SE, BSE, EBSD) (Fig. 8a-c), and analyzed by SIMS in 10 to 20 µm diameter spots to determine age, oxygen two- and three-isotope ratios, and trace element compositions. CL patterns of surfaces 3 and 4 reveal the core, which shows distinct concentric zoning (Fig. 8a). Surfaces 3 and 4 are the topic of this study and are interpreted to preserve the early Hadean history of the grain (Valley et al. 2014a). Age was measured six times on surface #3 (Cavosie et al., 2007; Valley et al. 2014a); pit locations are shown with dotted circles in the SE image of surface #4 (Fig. 8c). All three analyses of the core yield concordant overlapping U-Pb ages with an average ²⁰⁷Pb/²⁰⁶Pb age of 4374± 6 Ma (Figs. 8c, 9a, Table 1). Three analyses of the outer rim, where it is ~30 µm-thick, yield minor discordance and ²⁰⁷Pb/²⁰⁶Pb ages averaging 3400 Ma (Figs. 8c, 9a, Table 1). This rim age correlates to the intrusive age of the Dugel orthogneiss, which outcrops adjacent to the Jack Hills (3.38-3.35 Ga, Kinny and Nutman 1996; Pidgeon and Wilde 1998; Cavosie et al. 2004), but a more distant source can't be ruled out for this zircon.

The CL image of surface #4 shows more than one episode of dissolution and growth as is typical in igneous zircons. The innermost core (\sim 100 x 200 μ m) is off-center and truncated by

subsequent layers. The "mantle" of this grain (between the core and rim) shows concordant zoning that is locally cut by irregular disturbed domains that are dark and featureless in CL. The disturbed domains (D in Fig. 8a) show ~20% weaker diffraction by EBSD suggesting that they result from radiation damage (Valley et al. 2014a). The largest and most prominent disturbed domain measures ~30 x 150 μm. Surfaces #1 and 2 of this zircon expose the mantle region and the CL image shows multiple disturbed domains that may have compromised the earlier data (Fig. 1a in Cavosie et al. 2006). The outer rim of zircon JH4.4 is 10-30 μm thick, and cuts the earlier growth bands and disturbed domains, and preserves fine-scale zoning, suggesting an igneous origin. The outer form of this crystal is subhedral showing gentle (relative to some JH zircons) rounding from sedimentary transport. This zircon is broken at one end, in spite of using Electric Pulse Disaggregation, a relatively gentle, non-compressive method for disaggregating the host quartzite that yields fewer broken zircon fragments (Cavosie et al. 2004).

The BSE image of surface #4 (Fig. 8b) shows that most of the grain is zircon with subtle compositional zoning that correlates to CL. As is common in zircon, dark bands by CL are enriched in U, Th, Y and REEs causing them to be brighter by BSE. The disturbed domains are also bright in BSE, suggesting that they are likewise enriched in these elements. The prominent mineral inclusions are quartz, which is black in BSE (Fig. 8b) because the gain of the detector was adjusted to discriminate the small differences within zircon. The largest rounded quartz inclusion measured 50 x 100 µm in surface #3, but is smaller in Surface #4 (Fig. 8b). Xenotime inclusions are also identified by EDS (up arrows, bright BSE, bright CL). Several generations of fractures are seen including late hairline fractures with no visible mineralization and earlier cracks filled with quartz. Some cracks displace growth bands seen by CL. The displacement of CL bands by quartz-filled cracks locally offsets banding in the outer edge of the crystal (arrow, bottom edge of Fig. 8b), showing that these features postdate sedimentary abrasion of the zircon grain and probably result from burial and metamorphism of the host sandstone.

Slight misorientations of zircon crystal structure are also shown by EBSD in the lower right portion of the crystal (up to 8°, Valley et al. 2014a). The main portion of the crystal, including the core, is oriented with the [100] axis normal to the polished surface and parallel to the long axis of APT specimens. The domains of differing orientation are sharply bounded by visible brittle fractures. Some fractures are healed by zircon that is dark in CL and crystallographically oriented relative to adjacent zircon. Other cracks appear unhealed and may have formed later.

JH4.0

JH4.0 is a detrital zircon (01JH13b/2.5M/8-4) from metaconglomerate (sample 01JH13) in the Jack Hills, Western Australia. This sample is from the same 2-meter outcrop on Eranandoo Hill where samples W74 (Compston and Pidgeon 1986, Wilde et al. 2001) and 01JH-54 (Cavosie et al. 2004) were collected. The rock is a grey flattened-quartz-pebble metaconglomerate with accessory minerals including rutile, detrital zircon and chromite, bright-green metamorphic chromian-muscovite and monazite (Fig. 7b). A whole-rock XRF analysis of sample 01JH54, from the same layer as 01JH13, shows 94.9 wt% SiO₂ and 318 ppmw Zr (Cavosie et al. 2004).

The CL image of JH4.0 shows a dark disturbed core, a thin bright mantle that cuts both older and younger domains of the crystal and a concentrically zoned outer portion that is marked by multiple periods of resorption and growth as is common in igneous zircons. There is no single rim domain forming an overgrowth as in JH4.4, but the grain is highly rounded and it's impossible to evaluate by CL if a late overgrowth was removed by abrasion during sedimentary transport.

The ²⁰⁷Pb/²⁰⁶Pb age of zircon JH4.0 was measured from the concentrically zoned domain (Fig. 8d, e). The ²⁰⁷Pb/²⁰⁶Pb age is 4.007 Ga and the U/Pb ages are 97% concordant (Fig. 9b (Cavosie, 2005).

The δ^{18} O values of four spots in the concentrically zoned domain of JH4.0 average 5.9 $\pm 0.2\%$ (2SD) (Ushikubo et al. 2008). One analysis of the disturbed core yielded an unreliable value of 4.1%.

ARG2.5

ARG2.5 is the xenocrystic core of a zircon (ARG05-28-2) from granodiorite of the Vipoint pluton in the Grouse Creek Mountains, northern Utah. The Vipoint pluton represents one of four plutonic suites emplaced into the lower plate of the Albion - Raft River – Grouse Creek metamorphic core complex between 32 and 25 Ma (Strickland et al. 2011a, b). Zircons from sample ARG05-28 have igneous rims with average 206 Pb/ 238 U ages of 29.0 ± 0.3 Ma and inherited cores that range from 1.990 to 2.620 Ga. Monazite ages record sillimanite-grade metamorphism in wallrocks of the pluton synchronous with mid-crustal intrusion at ca. 32 to 27 Ma (Strickland et al. 2011a). These results indicate that in the Oligocene, zircon rims grew on Precambrian cores during a prolonged period of magmatic recycling and high-grade metamorphism in the mid-crust.

Zircon ARG2.5 has a core that is relatively dark by CL, but shows distinct concentric zoning in the domain dated at 2.542 Ga by SIMS and where the FIB lift out was made for APT (Fig. 8F). The lower part of this dark core has more complex zoning and was not sampled. The outer margin of the core was resorbed and is overgrown by a medium bright mantle, which is indistinguishable in age from the core (Figs. 8f and 9b) (Strickland et al. 2011a, Strickland pers. comm.). The thin outermost rim is brightest in CL and correlated to overgrowths that were dated at 29 Ma in other zircons from this sample.

The δ^{18} O values of the ARG05-28 zircons average 5.3 $\pm 0.5\%$ on their rims and 6.3 $\pm 0.5\%$ in their cores (Strickland et al. 2011b). Five APT specimens were milled from a FIB lift-out in the core of the zircon near the 2.542 Ga analysis spot (Valley et al. 2012).

Results

JH4.4

SIMS data

Oxygen isotope ratios were measured a total of 15 times in zircon and three times in quartz inclusions on surface #4 of JH4.4. Four zircon analyses included all three stable isotopes of oxygen making large, prominent ~30 x 40 x 2-µm pits. The oxygen three-isotope data plot along the Terrestrial Fractionation Line (TFL) in excellent agreement with other Jack Hills zircons and zircons from Earth in general (Valley et al. 2007, 2014a, Fig. 10). The deviation from TFL ($\Delta^{17}O = \delta^{17}O - 0.512\delta^{18}O$, Clayton 2007) is $0 \pm 0.2\%$, in excellent agreement with analyses of the KIM-5 zircon standard, which is a mantle megacryst from kimberlite (Valley et al. 1998, Page et al. 2007). Analysis of $^{18}O/^{16}O$ created smaller 10-µm pits (Fig. 8c). All analyses of the core and mantle except two that are in the dark disturbed zone average $\delta^{18}O = 4.8 \pm 0.6\%$. The four analyses of the zircon rim are distinctly higher, averaging $\delta^{18}O = 5.6 \pm 0.5\%$ (2SD). The two analyses of disturbed zircon were made on different days in oxygen 3-isotope and oxygen 2-isotope mode and are in perfect agreement, but over 1% lower in $\delta^{18}O$ (3.5, 3.6%). The accuracy of $\delta^{18}O$ values of the disturbed domain is not reliable due to lack of an appropriate standard and the compositions may not be primary.

The three SIMS analyses of quartz inclusions in zircon average $\delta^{18}O = 12.6 \pm 0.4\%$. For comparison, six analyses by laser fluorination of mm-size chips of the matrix quartz from the quartzite enclosing JH4.4 average $\delta^{18}O$ of 12.71 \pm 0.08% (2SD) Cavosie et al. 2005, App. 4).

Trace elements were measured by SIMS twice on surface 2, and three times in the core and once in the rim of surface 4. The 3.4 Ga rim of this zircon is distinctly different from the core.

REE concentrations are an order of magnitude lower than the other five spots, the Ce anomaly is larger, and the Eu anomaly is smaller (TE3, Fig. 11). The five REE analyses from the core and mantle of JH4.4 are similar with positive slopes and prominent positive Ce and negative Eu

anomalies. Values of [Ti] range from 10.0 to 18.4 ppm in the core of JH4.4 and one analysis of the rim is 2.5 ppm.

APT data

Two needle-shaped specimens were milled from the core of JH4.4 using standard site-specific focused ion beam (FIB) methods to dimensions of ca. 100 x 100 x >1500 nm and analyzed by APT as discussed by Valley et al. (2014a). A total of 600 million ions were detected; 2 x10⁸ from specimen 1 and 4 x10⁸ from specimen 2. The elemental and isotopic compositions within these specimens are bimodal with small 5-10 nm domains (clusters) concentrated in elements that are less compatible or incompatible within the crystal structure of zircon including Pb, Y, and REEs (Fig. 12). Concentrations of Y are as high as 8 at% in the centers of clusters and grade outward to lower values over <5nm (Fig. 13a). The location of clusters and their boundaries can be defined in various ways. In this sample, the contour for 3-at% Y is used. The average Y content inside the 3-at% contours surrounding clusters is 4.4 at% (10.5 wt%). The sum of Y + REEs totals over 20 wt% within the clusters (Table 3). Lead and P are also concentrated inside of the clusters, but at lower levels of 4600 and 1600 ppmw, respectively. Concentrations of Zr and Hf are lower in the clusters to compensate.

 spheres, but actual lengths are slightly longer. There is approximately one cluster per 100,000 nm³ of zircon in JH4.4 and the measured nearest-neighbor distance averages 22 nm, center-to-center.

There are three sets of clusters. Two sets are oblate spheroids with preferred crystallographic orientations that are evident in the rotating tomographic movies for domains with Y > 3at% (App. 1). One set of clusters is flattened perpendicular to the long axis of the specimens, which were milled parallel to one a-axis of JH4.4. The other set is normal to this a-axis, but the full orientation is not known. The third set of clusters form spheres. A qualitative determination based visual examination of the clusters suggests that there is about one third of each set and no consistent differences have been detected for chemistry or volume of these clusters, though the spheres are slightly smaller.

The two specimens of zircon JH4.4 yielded the largest data set of the three zircons that have been analyzed by APT (6 x10⁸ ions). A total of 15,591 atoms of 207 Pb and 206 Pb were detected after background correction (Table 4, not including the domains between the 1-at%-Y and 3-at%-Y contours). The signal/background ratio is 1.088 for 207 Pb and background correction is important. The 207 Pb/ 206 Pb ratio is 0.52 \pm 0.04 for the entire data set. For the combined volume of 319 clusters (defined by the 3-at%-Y contour), the 207 Pb/ 206 Pb ratio is 1.2 \pm 0.05 and the ratio for outside of clusters (less than 1-at%-Y) is 0.3 \pm 0.05 (Table 4). The concentric shell between 1 and 3% represents a mixture and yields ratio of ~1.15. Other contour intervals were investigated and for variations of \pm 0.5%-Y there is no significant difference in the measured 207 Pb/ 206 Pb ratios.

JH4.0

SIMS data

Trace elements were measured twice by SIMS in the concentrically zoned domain of JH4.0 (Bouvier et al. 2012) and [Li] plus δ^7 Li were measured four times including two analyses from

the core and mantle (Ushikubo et al. 2008) (Fig. 8e). For analyses in the concentrically zoned domain, concentrations of Li are uniformly high (45 to 56 ppmw) and values of δ^7 Li are low (-10 and -18‰). The specimens for APT analysis correlate most closely to REE analysis spot TE7 and are from a dark CL band that was selected as rich in Li. Li was mapped across this domain by SIMS. Note that intensity is reversed in figure 8d; brighter colors represent higher [Li] in the scanning ion image (inset) but zones that are enriched in Li, Y, REEs, U and Th are darker by CL (Ushikubo et al. 2008). The REEs are identical in both spots that were analyzed for trace elements. A chondrite normalized diagram shows a positive slope, and prominent positive Ce and negative Eu anomalies (Fig. 11, TE7 &8). Titanium varies from 6.1 to 7.7 ppm in these spots (Table 3).

APT data

APT specimens were obtained from the darkest undisturbed CL band of the concentrically zoned domain in JH4.0 (Fig. 8d) (Valley et al. 2012). Five specimens were analyzed by APT, yielding from 10 to 90 million ions each for a total of 2.15 x 10^8 . Peaks are prominent for Zr, Si, ZrO_x, and SiO_x (Fig. 4b). Several trace elements were identified including Li, P, Y, HREEs, Pb, and Hf. No zoning, heterogeneity or clusters are seen for these elements. There are no detectable spectral interferences for 6 Li⁺ and 7 Li⁺ (Fig. 5a). The measured concentration is 237 ppma (Table 3). Hydrides were not be evaluated, but will be less important for [Li] because 7 Li¹H is the more abundant hydride and [Li] is measured only at 6 and 7 Da. There were 6877 Pb ions detected with a 207 Pb/ 206 Pb ratio of 0.42 ±0.07 (2SD). Uncertainty of the Pb isotope ratio and for trace elements is larger than for the other zircons due to a low concentration of Pb, which is homogeneously dispersed within the specimens, causing a poor signal/background ratios (1.045 for 207 Pb).

ARG2.5

SIMS data

Trace elements were measured twice by SIMS, once in the core and once in the mantle of ARG2.5 (TE9 and TE10, Figs. 8f, 11). The REE patterns, like the ages, are similar for these two domains, showing a prominent positive Ce anomaly and flat HREEs. The negative Eu anomaly is muted for the mantle (TE9, Fig. 11). Titanium varies from 12.9 to 16.8 ppm. Analysis TE10 is from the same domain as the APT sample.

APT data

Four specimens were milled from ARG2.5 and analyzed by APT. From 9 to 35 million ions were counted from each specimen for a total of 7 x10⁷ ions (37% efficiency). There are prominent peaks are for Zr, Si, ZrO_x, and SiO_x. Several trace elements were identified including P, Y, HREEs, Hf, and Pb. The concentrations of Y, REE and Pb are strongly zoned in ARG2.5 and concentrated in clusters for all four specimens (Fig. 15).

The proximity histogram profile shows a radial distribution of enriched elements within the clusters. The greatest anomaly is in the center of each cluster (Fig. 13b). We define the boundaries of clusters by the 0.5-at%-Y contour for ARG2.5. The abundance of clusters varies significantly in the four specimens in comparison to the total number of ions detected (1 cluster for 9×10^6 ions, 15 for 10×10^6 ions, 20 for 16×10^6 ions, and 18 for 35×10^6 ions).

The clusters contain up to 4 at% Y and 1 at% Pb. This enrichment is mainly compensated by a decrease in Zr (Fig. 13b). The 3-D distribution of ²⁰⁷Pb and ²⁰⁶Pb is projected in figure 15b and includes a large contribution from background. It is significant that after background correction, all Pb is concentrated in the clusters and no Pb is detected outside the clusters (Fig. 6). In contrast, no zoning is seen in U or Th. Thus at nm-scale, the Pb is unsupported, meaning that the present locations of daughter atoms of Pb do not correlate to the locations of parent atoms of U and Th. In contrast, the SIMS data indicate that Pb is supported at µm-scale; Pb is radiogenic and

consistent with the concentrations of U and Th. This apparent contradiction also exists for the clusters in JH4.4 and will be discussed further after presentation of the Pb isotope ratios from APT and the effects of radiation damage.

Lead concentrations are higher in the clusters of ARG2.5 (\sim 1 at%) than in JH4.4 (0.08 at%) and the signal/background ratio is 2.0 for ^{207}Pb inside clusters, the highest seen in this study. These clusters are not homogeneously distributed throughout the volume investigated. One specimen with 1 x10 7 ions detected contains 13 clusters and another with 0.9 x10 7 ions contains only one. The ions-counted/cluster ratios vary by more than a factor of 10 (7.7 x10 5 to 9 x 10 6). Not, surprisingly, the smallest specimens have the extreme ratios; data for larger specimens average the grouped domains of variable cluster density. In spite of a smaller cumulative data set for ARG2.5 (7 x10 7 ions), the $^{207}\text{Pb}/^{206}\text{Pb}$ ratio can be estimated with higher precision in this zircon than in the older JH zircons because of higher signal/noise. Among the total ions counted in the Pb-rich clusters of the three specimens with more than one cluster from ARG2.5, there were 1135 ions of ^{206}Pb and 191 ions of ^{207}Pb detected for a $^{207}\text{Pb}/^{206}\text{Pb}$ ratio of 0.17 \pm 0.03 (2SD). Because all of the Pb detected in these specimens is concentrated in the clusters and no Pb is found outside the 0.5-at%-Y contour, this ratio represents the full volume of the specimens.

Discussion

Radiation Damage in Zircon

The clusters in JH4.4 and ARG2.5 are proposed to result from diffusion of incompatible elements into 5 to 10-nm-size amorphous domains created by alpha-particle recoil during U-series and Th-series radioactive decay (Valley et al. 2012, 2014a). The α -decay hypothesis has several testable consequences. During radioactive decay, each atom of 238 U, 235 U, or 232 Th begins a complex decay chain that includes 8, 7, or 6 α -decay events (and up to six β -decay events) culminating in daughter atoms of 206 Pb, 207 Pb and 208 Pb, respectively. For each α -decay, an α -

particle is emitted that travels distances of 10,000 to 20,000 nm, dissipates its energy through elastic collisions and causes a small number of atomic displacements (damage), mostly at its terminus. The more-massive newly formed daughter atom recoils 20-40 nm and creates approximately 10 times more damage that is highly concentrated where it stops, forming a small low-density amorphous domain surrounded by a halo of interstitials (Ewing et al. 2003). Thus, the decay of one atom of 238 U to 206 Pb proceeds through eight α -decay events (and six β -decay events) and a majority of the radiation damage is concentrated in eight sub-equant α -recoil domains that form sequentially, separated by distances of 20-40 nm/ each. BUT SEE JOCKHEERE 2001; KETCHAM ET AL. 2013

The dose of α -decay events experienced per unit weight of zircon can be calculated from the concentrations of U and Th, and the age. The calculated dose represents the total radiation emitted during the life of the zircon and would only represent the actually accumulated amount of damage in a zircon for the worst-case scenario where there is no annealing. Fortunately, zircons continuously self-heal at relatively low temperatures. Damage from α -recoil anneals at approximately the same temperatures as fission tracks, which are generally preserved in zircons only below 200-300°C (Davis and Krogh 2000; Nasdala et al. 2001b; Geisler et al. 2007). If damage in zircon is below the first percolation point, the amount of preserved radiation damage can be estimated from broadening and shifting towards lower wavenumber of Raman bands as measured in reflectance mode at 1- μ m-scale (Nasdala et al. 2001b; 2003; Pidgeon et al. 2013; Gao et al. 2014; Wang et al. 2014).

The calculated α -doses for zircons of this study are 4.44 x10¹⁵, 3.84 x10¹⁵, and 8.05 x10¹⁵ α -events/mg for the domains nearest to the APT-specimen lift-outs in JH4.4, JH4.0, and ARG2.5, respectively. The older zircons experienced less α -decay due to lower [U] and [Th]. In general, low [U] + [Th] below a few 100's of ppm is characteristic of zircons yielding concordant Archean or Hadean ages for this reason. The doses for the three sample zircons are all above the

first percolation point, and amorphous domains would form continuous pathways if all damage is retained, but that would be the case only if the zircons have been at low temperatures for most of their history.

Only part of the thermal history of the Jack Hills zircons is known. They have experienced the same temperatures since sedimentary deposition (ca. 3 Ga), including metamorphism at ~500°C at ca. 2.6 Ga. The earlier, predeposition histories of the detrital zircons are largely unconstrained. The SIMS data show that these concordant zircons have not lost Pb, which is consistent warm temperatures that prevented accumulation of high levels of radiation damage. However, higher doses and more radiation damage are commonly seen in zircons from 3.3 and 2.6 Ga granitoids adjacent to the Jack Hills metasediments (Pidgeon and Wilde 1998; Nasdala et al. 2001b; Utsunomiya et al. 2004, 2007) that may have had the same thermal history as the detrital Jack Hills zircons since 2.6 Ga. These metamict zones have significantly higher concentrations of U and Th than JH4.4 and JH4.0 and would have been more difficult to anneal, perhaps explaining the differences.

The low levels of radiation damage and the absence of Pb-mobility at the scale of a SIMS pit provides strong support for evaluating if compositions, including U-Pb-age, trace elements and δ^{18} O, are primary.

Genesis of Clusters

The clusters found in two of the three igneous zircons that have been analyzed to date by APT are attributed to reheating and diffusion into amorphous domains caused by α -recoil (Valley et al. 2012, 2014a). It is reasonable to consider explanations other than the α -recoil model for the genesis of these features.

Several observations indicate that the clusters are not caused by exsolution. The formula of the clusters in JH4.4 would be (Zr_{0.78}YREE_{0.38}P_{0.01}Si_{0.91}O₄) if APT data were normalized to four

oxygens. This cation-excess formula does not fit known zircon solid solutions or any other mineral. For instance, xenotime substitution requires P. The APT data rule out the presence of nano-crystals of ZrO₂ and SiO₂ that might form due to radiation damage. The clusters are best explained as originally forming non-stoichiometric amorphous zones within zircon that have become enriched in less compatible elements (but not U and P) at some time after formation of the zircon. It is likely that amorphous domains were partly annealed during prolonged metamorphism at 2.6 Ga, as seen by high-resolution HAAD-STEM (high-angle annular dark-field scanning transmission electron microscopy) in an undated detrital zircon from the same outcrop as JH4.0 (Utsunomiya et al. 2004).

Could the clusters in igneous zircons be primary? Zircons sometimes contain common Pb. which is generally concentrated in crystal defects or inclusions. The valence of Pb is 2+ for the oxygen fugacities typically found in the Earth's crust, and Pb²⁺ is too large (ionic radius 0.129 nm) to substitute for Zr⁴⁺ (0.084 nm) (Shannon 1976). Possibly, radiogenic Pb⁴⁺ (0.094 nm) substitutes during annealing into nano-domains within some zircons (Utsunomiya et al. 2004). For the zircons of this study, the possibility that common Pb was trapped in clusters at the time the zircon crystallized is tested by the ²⁰⁷Pb/²⁰⁶Pb ratios. In each of the three zircons, the ²⁰⁷Pb/²⁰⁶Pb ratios for the full volume of the APT specimens (within and outside of clusters) are within analytical error of the value for the much larger volume measured by SIMS (Table 4). The agreement of ²⁰⁷Pb/²⁰⁶Pb ratios measured by the two techniques and the low common Pb $(^{204}\text{Pb}/^{206}\text{Pb} < 1 \text{ x}10^{-4})$ measured by SIMS prove that the Pb formed by radioactive decay inside the zircon over an extended period of time. The ²⁰⁷Pb/²⁰⁶Pb ratio of 0.17 required 2.5 b.y. to form in ARG2.5. As discussed below, the surprisingly high ²⁰⁷Pb/²⁰⁶Pb ratio of 1.2 in clusters from JH4.4 suggests that radiogenic Pb was concentrated in clusters at 3.4 Ga following 1 b.y. of radioactive decay. In both of these zircons the ²⁰⁷Pb/²⁰⁶Pb ratios rule out the possibility that the clusters formed at the same time as the host zircons. For the volumes inside of clusters, Pb is

concentrated, but there is no comparable concentration of U and Th. Thus, the Pb is both radiogenic and unsupported by parent isotopes. Some process of concentration is required that operated after radioactive decay had formed the Pb.

One clue to the nature of cluster formation is the identity of other elements that are colocalized with Pb. For JH4.4, 12 elements were analyzed by APT and shown to be concentrated in the clusters. In addition to Y, eight heavy rare earth elements (HREEs), Pb, Al and Ca are present at higher levels in the clusters than in surrounding zircon (Table 3, Fig. 13a). The concentrations of Zr and Hf are lower to compensate. There may also be a small change in [Si]. A normalized plot of the eight HREEs parallels the SIMS data for these zircons (Fig. 11) with an average enrichment factor of 58. Terbium, which has the lowest concentration by SIMS of these eight HREEs (TE1 & TE2 average 27 ppm), is proportionately less enriched. The light REEs (LREEs), which have the lowest concentrations by SIMS (<18 ppm), were not detected by APT. The REEs and Y are less compatible in zircon at lower temperatures. Lead, Ca and Al are incompatible in zircon and often correlated with radioactive decay or damage (Rayner et al. 2005, Geisler et al. 2007). Thus these elements can show a preference to partition into crystal defects or amorphous domains more than zircon.

Timing of Zircon Crystallization and Cluster Formation

The timing of zircon crystallization and cluster formation is determined from the ²⁰⁷Pb/²⁰⁶Pb ratios. The APT and SIMS data are complementary and together give a more complete history than either data set alone. JH4.0 has no clusters and the ²⁰⁷Pb/²⁰⁶Pb ratios are the same by APT (0.42) and by SIMS (0.4269), consistent with the Pb/Pb model age of 4.007 Ga. For ARG2.5, the ²⁰⁷Pb/²⁰⁶Pb ratio of the entire specimen by APT is the same as in clusters because no Pb is detected outside of the clusters. This ratio by APT (0.17) yields a Pb/Pb model age of 2.5 Ga in excellent agreement with the ratio of 0.1684 measured by SIMS. The Pb/Pb model age indicates

Pb mobility from the matrix to clusters was recent. In other words, U- and Th-decay proceeded for 2.5 b.y. and then all of the radiogenic Pb migrated to the clusters. If Pb migration had been earlier, then the U and Th that remain outside of the clusters would have produced more Pb.

For JH4.4, the average ²⁰⁷Pb/²⁰⁶Pb ratio of the full APT specimens is 0.52, within uncertainty of 0.5472 measured by SIMS, and consistent with the Pb/Pb model age of 4.374 Ga, and the concordant U-Pb ages by SIMS. Outside of the clusters, the ratio is 0.3 by APT, within uncertainty of 0.2867 by SIMS and a model age of 3.4 Ga for the younger rim of the zircon. However, no SIMS data match this ratio (0.3) within the core of the zircon because the relatively large volume analyzed by SIMS homogenizes approximately one million clusters. Inside of the clusters, the ²⁰⁷Pb/²⁰⁶Pb ratio is 1.2, which is much higher than in SIMS data for any of the Hadean zircons. This ratio cannot be interpreted with a model age assuming recent Pb loss. A chord from the origin with this slope (dashed in Figure 9a) would indicate an age of ca. 5.5 Ga, which is older than the Earth and such a model is not correct. The calculation of a standard model age is not appropriate because (1) the Pb mobility was not recent, and (2) more critically, early-formed radiogenic Pb migrated into U-poor domains. The APT data only give a ²⁰⁷Pb/²⁰⁶Pb ratio, which defines the slope in figure 9a, but not the Y-intercept. If, instead of passing through the origin, a line with this slope is drawn from the crystallization age of 4.4 Ga determined by SIMS, then the lower intercept is at 3.4 Ga (dashed line in Fig. 9a), which is the age of the rimforming event. A model for zircon growth at 4.374 Ga and cluster formation at 3.4 Ga thus fits the data perfectly. The radiogenic Pb that formed between 4.374 and 3.4 Ga is enriched in ²⁰⁷Pb because there was proportionately more of the shorter-lived parent, ²³⁵U, on the early Earth. The ²⁰⁷Pb/²⁰⁶Pb ratio can be calculated, and for a zircon that crystallized at 4.374 Ga, the ratio will be 1.2 at 3.4 Ga, based on the half-lives of 238 U and 235 U, and the modern ratio of 238 U/ 235 U = 137.82. The agreement of measured and calculated ratios strongly supports the interpretation that JH4.4 crystallized at 4.374 and that 1 b.y. later, all of the radiogenic Pb migrated to the clusters.

Thus, the clusters in JH4.4 contain less Pb than clusters in ARG2.5 because of lower [U] and [Th], but also because they only represent 1 b.y. of radioactive decay vs. 2.5 b.y. From 3.4 Ga until today, radioactive decay has continued in JH4.4, creating a 207 Pb/ 206 Pb ratio of 0.3 outside of clusters, but the ratio has not been significantly changed inside the clusters due to the \sim 40-times higher ratio of [Pb]/ [U] + [Th].

The α-recoil Model

The α -recoil model (Valley et al. 2012, 2014a) proposes late migration of incompatible elements into amorphous domains caused by α -recoil at the time of high-grade reheating events. This model suggests several tests that could either strengthen or refute it. As discussed above, the decay chains for individual parent atoms of 238 U, 235 U or 232 Th will create groups of 8, 7, or 6 spatially related domains of α -recoil damage, respectively. Furthermore, these domains will form sequentially with predictable distances based on mineralogy, the energy of the daughter atom and possibly the crystallographic orientation of the recoil. Visual inspection of the rotating APT movies for clusters in JH4.4 and ARG2.5 shows clear variability in the density of clusters and is permissive of groups of 6 to 8, though many domains extend beyond the FIB-milled boundaries of the specimens and many groups are smaller than 6. The abundances of the three parent isotopes at the time of cluster formation further predict the proportions of different group size and groups of eight clusters should be most common. The size, abundance, and inter-cluster distances should all be consistent with this model, but the data set is not presently large enough to test this hypothesis.

The high [Pb] within clusters is not predicted if all domains of α -recoil damage are equally preserved. Only one atom of radiogenic Pb is produced for every 6-8 α -recoil events, yet the clusters in JH4.4 contain on average ~150 atoms of Pb/cluster and in ARG2.5, there are ~100 atoms of Pb/cluster. If the clusters are occupying domains of α -recoil, then less than 1 in 1000 α -

recoil events has resulted in a cluster. This is readily explained if the zircons were continuously annealed during their early history (consistent with concordant ages) and only a small percentage of damaged domains were amorphous at the time of reheating and mobilization of Pb.

If these zircons were continuously annealed, then the radiation damage never reached the first percolation point and volume diffusion through crystalline zircon is required to explain Pb and YREE migration into clusters. For the inter-cluster spacing of JH4.4 and ARG2.5, diffusion distances on the scale of 20 nm would be sufficient to concentrate less compatible elements in the amorphous domains created by α-recoil. Rates of Yb (and other REE) diffusion are predicted by experimental data (Cherniak 2010) and are too slow below 500°C to accomplish this concentration. However, heating to 800°C for ~2 m.y. would be sufficient for REEs to diffuse 20 nm. Pb diffusion is faster and any reheating that concentrated REEs could efficiently scavenge Pb. Compatible elements, including U and Th, have no energetic drive to diffuse. There is no younger rim on JH4.0, suggesting the lack of reheating and explaining the absence of clusters in this zircon. The igneous rims on grains JH4.4 (3.4 Ga) and ARG2.5 (29 Ma) document periods when these zircons were reheated as xenocrysts in younger magmas. Such magmatic recycling generally proceeds during high-grade metamorphism in the deep crust. This high temperature event is documented at 29 Ma when the rim of ARG2.5 formed in the crystallizing Vipoint pluton (Strickland et al. 2011a, b). Thus a Pb/Pb model age assuming recent Pb loss explains the ²⁰⁷Pb/²⁰⁶Pb ratio inside clusters. This model predicts the presence of ~2ppm of radiogenic Pb that formed over the past 29 m.y. in the regions outside of clusters, but this concentration is too small to be detected by APT. If the age of reheating was significantly older than 100 Ma, there should be Pb detected outside of the clusters by APT

The SIMS age for the rim on JH4.4 documents reheating at ca 3.4 Ga. In contrast to ARG2.5, JH4.4 is detrital, and the parent rock and field relations are unknown. The 3.4 Ga rim could be related to the intrusion of Dugel orthogneisses (3.38-3.35 Ga, Kinny and Nutman 1996; Pidgeon

and Wilde 1998; Cavosie et al. 2004) that outcrop adjacent to the Jack Hills or to igneous events elsewhere. The age of 3.4 Ga is indicated in two ways by the APT ²⁰⁷Pb/²⁰⁶Pb ratios. The ratio of 0.3 outside of the clusters requires 3.4 b.y. to accumulate. Likewise the unusually high ratio of 1.2 from inside of the clusters indicates a shorter period of radioactive decay early in Earth history, which, if it started at 4.374 Ga terminated 1 b.y. later at 3.4 Ga. Thus for both ARG2.5 and JH4.4, the age of the reheating event could be deduced from the APT results even if the younger rim was abraded away during sedimentary transport. More generally, APT data offer a new approach for identifying and constraining otherwise cryptic thermal events due to magmatism or high-grade metamorphism.

One final test of the α -recoil model relates to the annealing rate of radiation damage. It is generally agreed that long-term annealing of α -recoil damage begins at low temperatures and can be nearly complete above ~300°C, and yet volume diffusion distances of ~20 nm for REEs into the clusters suggest temperatures of ~800°C. How can the damaged domains survive in order to concentrate incompatible elements? The results discussed above indicate that the majority of recoil-damaged domains that formed in JH4.4 and ARG2.5 are not represented by clusters and thus were probably annealed before the reheating event. This suggests that temperatures were kept above 200-300°C and annealing was at steady state. In this scenario, new amorphous domains formed and were annealed continuously. Thus there was always a small population of newly formed unannealed domains and they persisted long enough to concentrate less compatible elements when reheating opened the zircon to short-distance diffusion. This prediction suggests that the time required to anneal α -recoil damaged domains is longer than the ~2 m.y. necessary for Pb and YREEs to diffuse 20 nm in zircon.

The process of radiation damage and annealing is not a reversible reaction and does not follow the same rate law as volume diffusion. Healing is a complex process that varies with the extent of damage and is faster under hydrous conditions (Pidgeon et al. 1966). Beam broadening

and peak shifts by Raman-spectroscopy show that both naturally and experimentally damaged zircons experience hysteresis in annealing. In addition to amorphous ZrSiO₄, oxides, micro-strain, voids, dislocation loops, and point defects can form (Ewing et al. 2003; Nasdala et al. 2003). As an extreme case, Geisler et al. (2001) estimate that recrystallization of fully metamict zircon could take 370 m.y. at 700°C, much longer than necessary to heal less damaged zircons, and far longer than the 2 my required to form clusters. Thus, the zircons of this study maintained a steady-state density of α -recoil damage below the first percolation over 100's to 1000's of m.y. and the relatively short reheating events were not sufficient to remove all of the constantly regenerating domains of α -recoil damage.

Fidelity of the zircon record

Cavosie et al. (2006) defined type-1 and type-2 domains within zircon based on chondritenormalized values of LREE measured by SIMS. Type-2 zircons (La>1 and Pr>10) are
interpreted as disturbed with REE mobility probably enhanced by radiation damage. The zircons
of this study are type-1 by this definition and do not show evidence for trace element mobility at
the 10-µm-scale of a SIMS analysis pit. The demonstration by APT that these ancient zircons
were closed systems to mobility of Pb and YREEs at the scale of SIMS analyses (10-25 um
spots) supports the conclusion that type-1 zircons preserve magmatic compositions and it
removes one of the long-lasting challenges to the accuracy of in situ U-Pb geochronology.
Furthermore, it provides greater confidence in the reliability of other geochemical measurements
in these zircons.

Oxygen Isotopes

Oxygen isotope ratios in zircons, measured in situ by SIMS can restrict the parent rock and its protolith as well as the later thermal and alteration history (Valley 2003). All $\delta^{18}O(Zrc)$ values

in the three grains studied are within uncertainty of mantle-like values, 4.7 to 5.9‰ (Table 2). Such primitive δ^{18} O values are common in the detrital Hadean suite, although many of the zircons are mildly elevated up to 7.5‰ (Fig.16) (Peck et al. 2001; Valley et al. 2005, Cavosie et al. 2005, 2007; Trail et al. 2007; Harrison et al. 2008).

In contrast to the primitive magmatic values in zircon, three analyses of disturbed domains within JH4.0 and JH4.4 are lower in δ^{18} O (4.1 to 3.5‰). Disturbed areas within zircon crystals frequently have distinctive CL patterns and can result from accumulated radiation damage that short-cuts diffusion and opens the crystal structure to exchange and alteration of primary δ^{18} O values (Valley et al. 2005; Cavosie et al. 2005). Alternatively, Pidgeon (1992) reports a similar CL texture for "unzoned" domains within zircons from a late granite cutting Jack Hills metasediments (W-34) and attributes it to subsolidus recrystallization synchronous to intrusion and metamorphism at ca. 2.6 Ga when the zircon was too young to have accrued significant radiation damage. The reduced crystallinity (as measured by EBSD) of disturbed domains in JH4.4 supports the radiation damage hypothesis for this grain (Valley et al. 2014a). Either way, disturbed domains cannot be assumed to preserve primary igneous compositions. Furthermore, accurate analysis by SIMS is not possible for metamict zircon without specific radiation-damaged standards that do not presently exist. In this study, the three δ^{18} O values for disturbed domains in JH4.4 will not be considered further.

Oxygen three isotopes, $\delta^{18}O$ and $\delta^{17}O$, have been measured in JH4.4 and JH4.0 and other Hadean zircons from the Jack Hills (Fig. 10) (Valley et al. 2007, 2014a). Values of $\Delta^{17}O$ are normalized relative to bulk silicate Earth (defined as $\Delta^{17}O = 0\%$ for the KIM-5 zircon standard, a mantle megacryst) and are precise to ± 0.22 (2SD, N=28, 2SE=0.04‰). Thirty-six zircons with ages from 4.0 to 4.35 Ga average $\Delta^{17}O = -0.05 \pm 0.24\%$ (2SD, N=44). The combination of $\Delta^{17}O = 0$, positive Ce anomaly, and low [Ti] provides a signature for terrestrial zircons (Valley et al. 2014b), ruling out an extra-terrestrial origin for the Jack Hills detrital zircons, including JH4.4

and JH4.0. These values reflect homogenization of the Earth following accretion, presumably by wholesale melting related to formation of the Moon and the Earth's core (Rumble et al. 2013; Valley et al. 2014a).

Conclusions

The complementary data from secondary ion mass spectrometry (SIMS) and atom probe tomography (APT) document atom-scale isotope and trace element distribution leading to enhanced understanding of thermal history of three Archean and Hadean zircons that have concordant U-Pb ages by SIMS of 2.5 to 4.4 Ga. APT shows that Pb, Y, and REEs are concentrated in 5-10 nm clusters in two zircons that have xenocryst cores and younger rims indicative of magmatic reheating. Quantitative measurements of the 207 Pb/ 206 Pb ratios provide nano-geochronological information. Lead in the clusters is radiogenic and unsupported by parent isotopes as predicted by the α -recoil model for their genesis. This model proposes that incompatible elements diffused into amorphous domains damaged by α -recoil during magmatic reheating (Valley et al. 2014a). The JH4.0 Ga zircon has no younger rim and contains no clusters ruling out magmatic reheating or high-grade metamorphism.

This first nano- and micro-geochronology study of multiple zircons provides enhanced confidence in the fidelity of their geochemical records. Demonstration that Pb mobility occurred at sub-50-nm scale to form clusters shows that longer-distance Pb transport did not occur and that the 20-µm-scale volumes interrogated by SIMS were closed systems. The existence of 4.4 Ga zircons, the oldest known from Earth, is confirmed. Likewise, REE spectra and stable isotope ratios are supported as primary, reflecting magmatic compositions. Taken together, these data support models of a more-clement Early Earth than the name Hadean suggests. Differentiated crust existed by 4.4 Ga, just 100 m.y. after the formation of the Moon and core. The steam

atmosphere cooled and precipitated as oceans before 4.3 Ga creating conditions habitable to life as much as 800 m.y. earlier than the oldest known microfossils.

More generally, the new tools are suited for minerals of all ages. The ability to analyze insulating as well as electrically conductive materials by APT bridges the gap in capabilities between TEM and SIMS. Single atoms in nano-domains, previously only imaged by TEM, can now be identified by mass and position. Conversely, zoning can be investigated in larger µmscale domains by SIMS, providing context for smaller-scale spatial information. These analytical advances open many new research opportunities of interest to mineralogists and geochemists.

Acknowledgements

The authors thank Brian Hess for sample preparation and polishing; John Fournelle and Phil Gopon for assistance with EPMA and SEM; Noriko Kita and Jim Kern for assistance with SIMS, and David Valley for assistance in fieldwork. John Craven assisted with SIMS analysis in Edinburgh and has been of invaluable assistance in many of the first author's *in situ* studies of oxygen isotope ratio. We thank Kouki Kitajima, Dunyi Liu, Des Moser, Mike Spicuzza, Simon Wilde, and many colleagues at CAMECA in Madison, Wisconsin for their contributions to these efforts. This research was supported by NSF-EAR0838058, DOE-93ER14389, and the NASA Astrobiology Institute. WiscSIMS is partly supported by NSF-EAR-1053466, -1355590.

References

Aines, R.D., and Rossman, G.R. (1986) Relationships between radiation damage and trace water in zircon, quartz, and topaz. American Mineralogist, 71(9-10), 1186-1193.

Bouvier, A.-S., Ushikubo, T., Kita, N.T., Cavosie, A.J., Kozdon, R. and Valley, J.W. (2012) Li isotopes and trace elements as a petrogenetic tracer in zircon: insights from Archean TTG's and sanukitoids. Contributions to Mineralogy and Petrology, 163, 745-768.

Cavosie, A.J. (2005) Geochemistry of > 3900 Ma detrital zircons from Jack Hills, Western Australia. PhD thesis, University of Wisconsin—Madison, 387 p.

Cavosie, A.J., Wilde, S.A., Liu, D., Valley, J.W., and Weiblen, P.W. (2004) Internal zoning and U-Th-Pb chemistry of the Jack Hills detrital zircons: a mineral record of early Archean to Mesoproterozoic (4348 -1576 Ma) magmatism. Precambrian Research, 135, 251-279.

Cavosie, A.J., Valley, J.W. and Wilde, S.A. (2005) Magmatic δ^{18} O in 4400-3900 Ma detrital zircons: A record of the alteration and recycling of crust in the Early Archean. Earth and Planetary Science Letters, 235, 663-681.

Cavosie, A.J., Valley, J.W., Wilde, S.A. and E.I.M.F. (2006) Correlated microanalysis of zircon: Trace element, δ^{18} O, and U-Th-Pb isotopic constraints on the igneous origin of complex >3900 Ma detrital grains. Geochimica et Cosmochimica Acta, 70, 5601-5616.

Cavosie, A.J., Valley, J.W., and Wilde, S.A. (2007) The oldest terrestrial mineral record: A review of 4400 to 4000 Ma detrital zircons from the Jack Hills, Western Australia. In: M.J. van Kranendonk, R.H. Smithies, V.C. Bennett (eds). Earth's Oldest Rocks. Developments in Precambrian Geology, 15, 91-111.

Chakoumakos, B.C., Murakami, T., Lumpkin, G.R., and Ewing, R.C. (1987) Alpha-Decay—Induced Fracturing in Zircon: The Transition from the Crystalline to the Metamict State. Science, 236 (4808), 1556-1559.

Cherniak, D.J. (2010) Diffusion in accessory minerals: zircon, titanite, apatite, monazite and xenotime. Reviews in Mineralogy and Geochemistry, 72, 827-869.

Clayton, R.N. (2007) Oxygen isotopes in meteorites, Treatise on Geochemistry, 1, 1–14.

Compston, W.T. and Pidgeon, R.T. (1986) Jack Hills, evidence of more very old detrital zircons in Western Australia. Nature, 321, 766-769.

Condon. D.J. and Schmitz, M.D. (eds.) (2013) One hundred years of geochronology. Elements, 9, 3-80.

- Corfu, F., Hanchar, J.M., Hoskin, P.W., and Kinny, P. (2003) Atlas of zircon textures. Reviews in Mineralogy and Geochemistry, 53, 469-500.
- Currie, L. A. (1968) Limits for Qualitative Detection and Quantitative Determination: Application to Radiochemistry. Analytical Chemistry, 40, 586–592.
- Davis, D.W., and Krogh, T.E. (2000) Preferential dissolution of sup 234 / sup U and radiogenic Pb from α-recoil-damaged lattice sites in zircon: implications for thermal histories and Pb isotopic fractionation in the near surface environment. Chemical Geology, 172(1), 41-58.
- Dobrzhinetskaya, L., Wirth, R., and Green, H. (2014) Diamonds in Earth's oldest zircons from Jack Hills conglomerate, Australia, are contamination. Earth and Planetary Science Letters, 387, 212-218.
- Ewing, R.C., Meldrum, A., Wang, L., Weber, W.J. and Corrales, L.R. (2003) Radiation effects in zircon. Reviews in Mineralogy and Geochemistry, 53, 387-425.
- Fu, B., Page, F.Z., Cavosie, A.J., Fournelle, J., Kita, N.T., Lackey, J.S., Wilde, S.A. and Valley, J.W. (2008) Ti-in-zircon thermometry: applications and limitations. Contributions to Mineralogy and Petrology, 156, 197-215.
- Gao, Y.Y., Li, X.H., Griffin, W.L., O'Reilly, S.Y., and Wang, Y.F. (2014) Screening criteria for reliable U–Pb geochronology and oxygen isotope analysis in uranium-rich zircons: A case study from the Suzhou A-type granites, SE China. Lithos, 192, 180-191.
- Gault, B., Moody, M.P., Cairney, J.M., and Ringer, S.P. (2012) Atom Probe Microscopy. Springer Series in Materials Science, Springer Series in Materials Science, 160, 396 p.
- Geisler, T., and Schleicher, H. (2000) Improved U–Th–total Pb dating of zircons by electron microprobe using a simple new background modeling procedure and Ca as a chemical criterion of fluid-induced U-Th-Pb discordance in zircon. Chemical Geology, 163, 269-285.
- Geisler, T., Pidgeon, R.T., Kurtz, R., van Bronswijk, W., and Schleicher, H. (2003) Experimental hydrothermal alteration of partially metamict zircon. American Mineralogist, 88, 1496-1513.
- Geisler, T., Schaltegger, U., Tomaschek, F., 2007. Re-equilibration of zircon in aqueous fluids and melts. Elements 3, 43–50.
- Geisler, T., Ulonska, M., Schleicher, H., Pidgeon, R.T. and van Bronswijk, W. (2001) Leaching and differential recrystallization of metamict zircon under experimental hydrothermal conditions. Contributions to Mineralogy and Petrology, 141, 53-65.
- Harrison, T.M. (2009) The Hadean crust: evidence from > 4 Ga zircons. Annual Review of Earth and Planetary Sciences, 37, 479-505.
- Harrison, T.M., Schmitt, A.K., McCulloch, M.T. and Lovera, O.M. (2008) Early (≥ 4.5 Ga) formation of terrestrial crust: Lu–Hf, δ^{18} O, and Ti thermometry results for Hadean zircons. Earth and Planetary Science Letters, 268, 476-486.

Heck, P.R., Staderman, F.J., Isheim, D., Auciello, O., Daulton, T.L., Davis, A.M., Elam, J.W., Floss, C., Hiller, J., Larson, D.J., Lewis, J.B., Mane, A., Pellin, M.J., Savina, M.R., Seidman, D.N., and Stephan, T. (2014) Atom-probe analyses of nanodiamonds from Allende. Meteoritics and Planetary Science. Doi: 10.1111/maps.12265.

Hellman, O.C., Vandenbroucke, J.A., Rusing, J., Isheim, D. and Seidman, D.N. (2000) Analysis of three-dimensional atom-probe data by the proximity histogram. Microscopy and Microanalysis, 6, 437–444.

Holmes, A. (1913) The Age of the Earth. Harper and Brothers, London. 196 p.

Hopkins, M., Harrison, T.M. and Manning, C.E. 2008. Low heat flow inferred from >4 Ga zircons suggests Hadean plate boundary interactions. Nature, 456, 493–496.

Hopkins, M.D., Harrison, T.M., and Manning, C.E. (2010). Constraints on Hadean geodynamics from mineral inclusions in > 4Ga zircons. Earth and Planetary Science Letters, 298, 367-376.

Hoskin, P.W. (2005) Trace-element composition of hydrothermal zircon and the alteration of Hadean zircon from the Jack Hills, Australia. Geochimica et Cosmochimica Acta, 69, 637-648.

Hoskin, P.W., and Schaltegger, U. (2003) The composition of zircon and igneous and metamorphic petrogenesis. Reviews in Mineralogy and Geochemistry, 53(1), 27-62.

Kellogg, G.L. and Tsong, T.T. (1980) Pulsed-laser atom-probe field-ion microscopy. Journal of Applied Physics, 51, 1184-1194.

Kelly, T.F. and Larson D.J. (2012) Atom probe tomography Annual Review of Materials Research, 42, 1-31.

Kelly, T. F., Voelkl, E. & Geiser, B. P. (2009) Practical Determination of Spatial Resolution in Atom Probe Tomography. Microscopy and Microanalysis, 15, 12–13.

King, E.M., Valley, J.W., Davis, D.W. and Edwards, G.R. (1998) Oxygen isotope ratios of Archean plutonic zircons from granite–greenstone belts of the Superior Province: indicator of magmatic source. Precambrian Research, 92, 365-387.

Kinny, P.D. and Nutman, A.P. (1996) Zirconology of the Meeberrie gneiss, Yilgarn Craton, Western Australia: an early Archean migmatite. Precambrian Research, 78, 165–178.

Kita N.T., Ushikubo, T., Fu, B. and Valley, J.W. (2009) High precision SIMS oxygen isotope analyses and the effect of sample topography. Chemical Geology, 264, 43-57.

Krogh, T.E. (1982) Improved accuracy of U-Pb zircon ages by the creation of more concordant systems using an air abrasion technique. Geochimica et Cosmochimica Acta, 46(4), 637-649.

Krogh, T.E., and Davis, G.L. (1975) Alteration in zircons and differential dissolution of altered and metamict zircon. Carnegie Institute of Washington Yearbook, 74, 619-623.

Kunicki T.C., Beerman D., Geiser B.G., Oltman E., O'Neill R.W., and Larson D.J. (2006) Atom probe data reconstruction, visualization and analysis with the Imago Visualization and Analysis

- System (IVAS). Proceedings, 19th International Vacuum Nanoelectronics Conference & 50th International Field Emission Symposium. 535–536.
- Kusiak, M.A., Whitehouse, M.J., Wilde, S.A., Nemchin, A.A. and Clark, C. (2013a) Mobilization of radiogenic Pb in zircon revealed by ion imaging: Implications for early Earth geochronology. Geology, 41, 291-294.
- Kusiak, M.A., Whitehouse, M.J., Wilde, S.A., Dunkley, D.J., Menneken, M., Nemchin, A.A., and Clark, C. (2013b) Changes in zircon chemistry during Archean UHT metamorphism in the Napier Complex, Antarctica. American Journal of Science, 313(9), 933-967.
- Larson, D.J., Alvis, R.A., Lawrence, D.F., Prosa, T.J., Ulfig, R.M., Reinhard, D.A., Clifton, P.H., Gerstl, S.S.A., Bunton, J.H., Lenz, D.R., Kelly, T.F., and Stiller, K. (2008) Analysis of bulk dielectrics with atom probe tomography. Microscopy and Microanalysis, 14, 1254-1255.
- Larson, D. J., Gault, B., Geiser, B. P., De Geuser, F. & Vurpillot, F. (2013) Atom Probe Tomography Spatial Reconstruction: Status and Directions. Current Opinion in Solid State and Materials Science, 17, 236–247.
- Larson, D.J., Prosa, T.J., Ulfig R.M., Geiser B.P. and Kelly, T.F. (2013) Local Electrode Atom Probe Tomography: A User's Guide. Springer, Heidelberg. 318 p.
- Ludwig, K.R. (2001a). Isoplot/Ex 2.49. Berkley Geochronology Center.
- Ludwig, K.R. (2001b). SQUID 1.02, A User's Manual; Berkeley Geochronology Center Special Publication no. 2. Review June, 20, 19.
- Mattinson, J.M. (2005) Zircon U–Pb chemical abrasion ("CA-TIMS") method: combined annealing and multi-step partial dissolution analysis for improved precision and accuracy of zircon ages. Chemical Geology, 220, 47-66.
- Miller, M. K., Russell, K. F., Thompson, K., Alvis, R. & Larson, D. J. (2007) Review of Atom Probe FIB-Based Specimen Preparation Methods. Microscopy and Microanalysis, 13, 428–436.
- Mojzsis, S.J., Harrison, T.M., and Pidgeon, R.T. (2001) Oxygen-isotope evidence from ancient zircons for liquid water at the Earth's surface 4,300 Myr ago. Nature, 409, 178-181.
- Nasdala, L., Beran, A., Libowitzky, E. and Wolf, D. (2001a) The incorporation of hydroxyl groups and molecular water in natural zircon (ZrSiO₄). American Journal of Science, 301, 831-857.
- Nasdala, L., Wenzel, M., Vavra, G., Irmer, G., Wenzel, T. and Kober, B. (2001b) Metamictisation of natural zircon: accumulation versus thermal annealing of radioactivity-induced damage. Contributions to Mineralogy and Petrology, 141, 125-144.
- Nasdala, L., Zhang, M., Kempe, U., Panczer, G., Gaft, M., Andrut, M., and Plötze, M. (2003). Spectroscopic methods applied to zircon. Reviews in Mineralogy and Geochemistry, 53, 427-467.

Nelson, D. R., Robinson, B. W., & Myers, J. S. (2000) Complex geological histories extending for≥ 4.0 Ga deciphered from xenocryst zircon microstructures. Earth and Planetary Science Letters, 181, 89-102.

Nemchin, A.A., Pidgeon, R.T. and Whitehouse, M.J. (2006). Re-evaluation of the origin and evolution of> 4.2 Ga zircons from the Jack Hills metasedimentary rocks. Earth and Planetary Science Letters, 244, 218-233.

Ortiz, D.M. (2010) Mineral inclusions in zircons: A tool for provenance analysis of sedimentary rocks. M.S thesis. University of Wisconsin, Madison. 47 p.

Page F.Z., Fu B., Kita N.T., Fournelle J., Spicuzza M.J., Schulze D.J., Viljoen V., Basei M.A.S. and Valley J.W. (2007) Zircons from kimberlites: New insights from oxygen isotopes, trace elements, and Ti in zircon thermometry. Geochimica et Cosmochimica Acta, 71, 3887-3903.

Panayi, P. (2012) Curved Reflectron. US Patent No. 8,134,119 and UK 0509638.3.

Parrish, R.R. and Noble, S.R. (2003) Zircon U-Th-Pb geochronology by isotope dilution—thermal ionization mass spectrometry (ID-TIMS). Reviews in Mineralogy and Geochemistry, 53, 183-213.

Peck, W.H., Valley, J.W., Wilde, S.A., Graham, C.M. (2001) Oxygen isotope ratios and rare earth elements in 3.3 to 4.4 Ga zircons: Ion microprobe evidence for high δ^{18} O continental crust and oceans in the Early Archean. Geochimica et Cosmochimica Acta. 65, 4215-4229.

Pidgeon, R.T. (1992) Recrystallization of oscillatory zoned zircon: some geochronological and petrological implications. Contributions to Mineralogy and Petrology, 110, 463–472.

Pidgeon, R.T. and Wilde, S.A. (1998) The interpretation of complex zircon U–Pb systems in Archaean granitoids and gneisses from the Jack Hills, Narryer Gneiss Terrane, Western Australia. Precambrian Research, 91, 309-332.

Pidgeon, R.T., O'Neil, J.R. and Silver, L.T. (1966). Uranium and lead isotopic stability in a metamict zircon under experimental hydrothermal conditions. Science, 154, 1538-1540.

Pidgeon, R.T., Furfaro, D., Kennedy, A.K., Nemchin, A.A., Van Bronswijk, W., and Todt, W.A. (1994) Calibration of zircon standards for the Curtin SHRIMP II. In Eighth International Conference on Geochronology, Cosmochronology and Isotope Geology: US Geological Survey Circular, 1107, 251.

Pidgeon, R.T., Nemchin, A.A., & Cliff, J. (2013) Interaction of weathering solutions with oxygen and U–Pb isotopic systems of radiation-damaged zircon from an Archean granite, Darling Range Batholith, Western Australia. Contributions to Mineralogy and Petrology, 166, 511-523.

Rasmussen, B., Fletcher, I.R., Muhling, J.R., Gregory, C.J. and Wilde, S.A. (2011) Metamorphic replacement of mineral inclusions in detrital zircon from Jack Hills, Australia: Implications for the Hadean Earth. Geology, 39, 1143-1146.

- Rayner, N., Stern, R.A., and Carr, S.D. (2005) Grain-scale variations in trace element composition of fluid-altered zircon, Acasta Gneiss Complex, northwestern Canada. Contributions to Mineralogy and Petrology, 148, 721-734.
- Reddy, S.M., Timms, N.E., Trimby, P., Kinny, P.D., Buchan, C., and Blake, K. (2006) Crystal-plastic deformation of zircon: A defect in the assumption of chemical robustness. Geology, 34(4), 257-260.
- Rios S., Salje, E.K.H., Zhang, M. and Ewing, R.C. (2000) Amorphization in zircon: evidence for direct impact damage. Journal of Physics: Condensed Matter, 12, 2410-2412.
- Rumble, D., Bowring, S., Iizuka, I, Komiya, T., Lepland, A., Rosing, M.T. and Ueno, Y. (2013) The oxygen isotope composition of Earth's oldest rocks and evidence of a terrestrial magma ocean. Geochemistry Geophysics Geosystems, 14, 1929-1939.
- Salje, E.K.H., Chrosch, J. and Ewing, R.C. (1999) Is "metamictization" of zircon a phase transition? American Mineralogist, 84, 1107-1116.
- Shannon, R.D. (1976) Revised effective ionic radii and systematic studies of interatomic distances in halides and chalcogenides. Acta Crystallographica Section A, 32, 751-767.
- Silver, L.T. (1963) The relation between radioactivity and discordance in zircons. National Academy of Science Publication, 1075, 34-39.
- Silver L. T., & Deutsch, S. (1963) Uranium-lead isotopic variations in zircons: a case study. Journal of Geology, 71, 721-758.
- Snoeyenbos, D., Jercinovic, M.J., Reinhard, D.A. and Hombourger, C. (2012) Characterization of minerals of geochronological interest by EPMA and atom probe tomography. American Geophysical Union Abstract V23C-2830.
- Stephenson, L. T., Moody, M. P., Gault, B. & Ringer, S. P. (2011) Estimating the Physical Cluster-Size Distribution within Materials Using Atom-Probe. Microscopy Research and Technique, 74, 799–803.
- Strickland, A., Miller, E.L. and Wooden, J.L. (2011a) The timing of Tertiary metamorphism and deformation in the Albion–Raft River–Grouse Creek metamorphic core complex, Utah and Idaho: The Journal of Geology, 119, 185–206.
- Strickland, A., Miller, E.L., Wooden, J.L. and Valley, J.W. (2011b) Syn-extensional plutonism and peak metamorphism in the Albion-Raft-River-Grouse Creek metamorphic core complex. American Journal of Science, 311, 261-314.
- Trail, D., Mojzsis, S.J., Harrison, T.M., Schmitt, A.K., Watson, E.B. and Young, E.D. (2007) Constraints on Hadean zircon protoliths from oxygen isotopes, Ti-thermometry, and rare earth elements. Geochemistry, Geophysics, Geosystems, 8(6).
- Tsong, T.T, Kinkus, T.J. and Al, C.F. (1983) Field induced and surface catalyzed formation of novel ions: A pulsed-laser time-of-flight atom-probe study. Journal of Chemical Physics. 78, 4763-4775.

Ushikubo, T., Kita, N.T., Cavosie, A.J., Wilde, S.A., Rudnick, R.L. and Valley, J.W. (2008) Lithium in Jack Hills zircons: Evidence for extensive weathering of Earth's earliest crust. Earth and Planetary Science Letters, 272, 666-676.

Utsunomiya, S., Palenik, C.S., Valley, J.W., Cavosie, A.J., Wilde, S.A., Ewing, R.C. (2004) Nanoscale occurrence of Pb in an Archean zircon. Geochimica et Cosmochimica Acta, 68, 4679-4686.

Utsunomiya, S., Valley, J.W., Cavosie, A.J., Wilde, S.A., and Ewing, R.C. (2007) Radiation damage and alteration of zircon from a 3.3 Ga porphyritic granite from the Jack Hills, Western Australia. Chemical Geology, 236, 92-111.

Valley, J.W. (2003) Oxygen isotopes in zircon. In: Hanchar, JM and Hoskin, PWO (eds) Zircon. Reviews in Mineralogy and Geochemistry, 53, 343-385.

Valley, J.W. (2006) MSA Presidential Address: New Tools For Old Minerals. Geological Society of America Annual Meeting, 38, 377.

Valley J (2010) Magmatic Zircons: Evolution of δ^{18} O Through Time – Revisited in situ. Goldschmidt Conference, Geochimica et Cosmochimica Acta, Suppl. 74, A1069.

Valley, J.W. and Graham, C.M. (1991) Ion microprobe analysis of oxygen isotope ratios in metamorphic magnetite-diffusion reequilibration and implications for thermal history. Contributions to Mineralogy and Petrology, 109, 38-52.

Valley, J.W. and Kita, N.T. (2009) *In situ* oxygen isotope geochemistry by ion microprobe, In: Fayek M. (ed) Mineralogical Association of Canada Short Course: Secondary Ion Mass Spectrometry in the Earth Sciences, 41, 19-63.

Valley, J.W., Bindeman, I.N. and Peck, W.H. (2003) Empirical calibration of oxygen isotope fractionation in zircon. Geochimica et Cosmochimica Acta, 67, 3257-3266.

Valley, J.W., Graham, C.M., Harte, B., Kinny, P. and Eiler, J.M. (1998) Ion microprobe analysis of oxygen, carbon, and hydrogen isotope ratios. In: McKibben, M.A., Shanks W.C. III, Ridley, W.I. (eds), Society of Economic Geology, Reviews in Economic Geology, 7, 73-98.

Valley, J.W., Lackey, J.S., Cavosie, A.J., Clechenko, C.C., Spicuzza, M.J., Basei, M.A.S., Bindeman, I.N., Ferreira, V.P., Sial, A.N., King, E.M., Peck, W.H., Sinha, A.K. and Wei, C.S. (2005) 4.4 billion years of crustal maturation: Oxygen isotopes in magmatic zircon. Contributions to Mineralogy and Petrology, 150, 561-580.

Valley, J.W., Ushikubo, T., and Kita, N.T. (2007) In situ analysis of three oxygen isotopes and OH in ALH 84001: Further evidence of two generations of carbonates. Lunar and Planetary Science Conference, 38, abstract #1147.

Valley JW, Ushikubo T, Strickland A, Reinhard DA, Snoeyenbos D, Lawrence D, Martin I, Kelly TF, and Cavosie AC (2012) Elemental and Isotopic tomography at single-atom-scale in 4.0 and 2.4 Ga zircons. Fall Meeting, AGU, San Francisco Abstract # V12A-05.

Valley, J.W., Cavosie, A.J., Ushikubo, T., Reinhard, D.A., Lawrence, D.F., Larson, D.J., Clifton, P.H., Kelly, T.F., Wilde, S.A., Moser, D.E. and Spicuzza, M.J. (2014a) Hadean age for a post-magma ocean zircon confirmed by atom-probe tomography. Nature Geoscience, 7, 219-223.

Valley, J.W., Spicuzza, M.J. and Ushikubo, T. (2014b) Correlated $\delta^{18}O$ and [Ti] in Lunar zircons: A terrestrial perspective for magma temperatures and water content on the Moon. Contributions to Mineralogy and Petrology, 167: doi:10.1007/s00410-013-0956-4

Wang, X.-L., Coble, M., Valley, J.W., Shu, X.-J., Kitajima, K., Spicuzza, M.J. and Sun, T. (2014) Influence of radiation damage on Late Jurassic zircons from Southern China: evidence from *in situ* measurements of oxygen isotopes, laser Raman, U-Pb ages, and trace elements. In review.

White, L.T., and Ireland, T.R. (2012) High-uranium matrix effect in zircon and its implications for SHRIMP U–Pb age determinations. Chemical Geology, 306, 78-91.

Whitehouse, M.J. and Kamber, B.S. (2002) On the overabundance of light rare earth elements in terrestrial zircons and its implication for Earth's earliest magmatic differentiation. Earth and Planetary Science Letters, 204, 333-346.

Wilde, S.A., Valley, J.W., Peck, W.H. and Graham, C.M. (2001) Evidence from detrital zircons for the existence of continental crust and oceans on the Earth 4.4 Gyr ago. Nature, 409, 175-178.

Williams, I.S. (1998) U–Th–Pb geochronology by ion microprobe. In: McKibben, M.A., Shanks W.C. III, Ridley, W.I. (Eds.), Applications of Microanalytical Techniques to Understanding Mineralizing Processes. Reviews in Economic Geology, 7, 1–35.

Figures

- Commonly achieved spatial resolution and detection range for microanalysis. APM atom probe microscopy; APT atom probe tomography; EDS energy dispersive X-ray spectrometry; EELS electron energy loss spectroscopy; EPMA electron probe micro analysis; SEM scanning electron microscopy; SIMS secondary ion mass spectrometry;
 (S)TEM scanning transmission electron microscopy; TOF time of flight; WDS wavelength dispersive X-ray spectrometry. (modified from Gault et al. 2012).
- 2. Milling of zircon needle-shaped specimens for APT by focused ion beam (FIB). (a) FIB lift-out from polished surface of JH4.0. (b) roughly milled tip. (c) and (d) sharpened tips with radius of curvature < 100 nm.
- (a) Schematic drawing of the CAMECA LEAP (local-electrode atom probe) instrument.(b) Schematic of the LEAP 4000HR instrument used in this study with a curved reflectron to enhance mass resolving power.
- 4. APT mass spectra from 1 to 130 Da for the three zircons of this study. (a) JH4.4. (b) JH4.0.(c) ARG2.5. Many elements form molecules and have multiple charge states, see text.
- 5. (a) APT mass spectrum at 6-7 Da and projection of atoms for Li in one needle-shaped specimen of JH4.0. (b) Mass spectrum at 16-18 Da showing peaks for three isotopes of oxygen and hydrides, see text.
- 6. APT mass spectra from 103-105 Da in ARG2.5. (a) Spectra for ions coming from volumes within clusters. (b) Spectra for ions from outside of clusters. Peaks at 103 and 103.5 Da are for ²⁰⁶Pb⁺⁺ and ²⁰⁷Pb⁺⁺. The peak at 104 Da is for ²⁰⁸Pb⁺⁺ and ²⁸Si₂¹⁶O₃⁺ inside of clusters and Si₂O₃⁺ only for outside of clusters, where there is no measurable Pb. The peak at 105 Da is singly substituted (²⁹Si or ¹⁷O) Si₂O₃⁺.

- 7. Photographs of polished rock surfaces from Jack Hills, Western Australia. (a) Metasandstone sample 01JH36 from which zircon JH4.4 was separated. (b) Meta-conglomerate sample 01JH13 from which zircon JH4.0 was separated.
- 8. SEM images of the three zircons in this study. (a) CL image of surface 4 in JH4.4 showing concentric banding of the core and 10-30-μm rim. The white rectangle near the center of the grain is the location of the FIB lift-out for APT specimens. D marks disturbed domains. (b) BSE image of surface 4 in JH4.4 showing inclusions of quartz (black) and xenotime (bright, up arrows). Brighter bands contain more REEs, Y and Pb. Four large 20 x 30 μm SIMS pits were for oxygen 3 isotopes. (c) Composite BSE-SE image of surface 4 of JH4.4 showing the locations of all SIMS measurements on surfaces 3 and 4. (d & e) CL and SE images of JH4.0 showing concentric banding, a dark disturbed core and the locations of SIMS analysis pits. The inset in (d) shows a scanning ion image of [Li] from the area around the APT sample locality; brighter colors are Li-richer. (f) CL image of ARG2.5 showing concentric zoning and the location of SIMS pits and APT specimens.
- 9. U-Pb concordia diagrams for 3 zircons. (a) Three analyses from the core of JH4.4 are concordant and overlap with an average age of 4.374 ±0.006 Ga. Three analyses on the rim yield Pb-Pb age of 3.4 Ga. The measured ²⁰⁷Pb/²⁰⁶Pb ratio of 1.2 from within clusters defines the slope shown by dashed lines. This is not interpreted as a conventional Pb/Pb age as projected from the origin (5.5 Ga), but rather as the composition of Pb that was concentrated in clusters at 3.4 Ga during reheating. (b) Nearly concordant analyses nearest to the APT specimens in JH4.0 and ARG2.5.
- 10. Oxygen three-isotope plot for Hadean zircons from the Jack Hills, including JH4.4 and JH4.0. All analyses fall within analytical uncertainty of the terrestrial fractionation line (TFL) as defined for bulk silicate Earth by mantle-derived zircons (blue). One spot on JH4.4 was of a disturbed domain (D) that yielded a lower δ^{18} O, but still plots on the TFL.

- 11. Chondrite-normalized plot of rare-earth elements (REEs) analyzed by SIMS from JH4.4, JH4.0, and ARG2.5, and by APT from JH4.4.
- 12. Atom Probe Tomography (APT) showing the distribution of Y and Pb atoms within a 1000-nm-long needle-shaped specimen of JH4.4. (a) Y projected for the full volume of the specimen. The smallest orange spots are individual Y atoms; the larger orange domains are ~10-nm clusters of Y atoms. (b) Enlarged view showing clusters of Y atoms (top). Clusters of Pb are obscured because data are projected through the ~100 nm thick specimens (bottom). (c) Enlarged view of Y, ²⁰⁷Pb and ²⁰⁶Pb in one cluster from (b). These images can be viewed as rotating movies in App. 1.
- 13. Radial distribution histograms of clusters in JH4.4 (a) and ARG2.5 (b). The clusters in JH4.4 (a) contain up to 8 at% Y and concentrations of Pb, HREE including Yb. For quantitative analysis and imaging of clusters, the volume inside clusters is set by the contour interval of 3 at% Y, and the volume outside of clusters is set by 1at% Y. In ARG2.5 (b), clusters contain up to 4 at% Y and 1 at% Pb with co-localized concentrations of HREE, and smaller increases in P and Al. The volume inside of clusters is set by the contour for 0.5 at% Y. [Zr] is less in both sets of clusters to compensate for increases of Pb and YREEs.
- 14. (a) Histogram of cluster volumes. The upper and lower boundaries of single clusters are an interpretation based on this distribution. (b) Histogram of the distances from the center of each cluster to the center of its nearest neighboring cluster.
- 15. Atom Probe Tomography (APT) showing the distribution of Y and Pb atoms within a 250-nm-long needle-shaped specimen of Arg2.5. (a) Single atoms and clusters of Y. (b) Single atoms and clusters of Pb. (c) Domains with >0.5 at% Y. These images can be viewed as rotating movies in App. 1.

16. Values of $\delta^{18}O$ for magmatic of zircons with low-radiation-damage vs. U-Pb age. Laser data were analyzed for $\delta^{18}O$ by bulk fluorination of ~ 2mg samples (typically a few hundred zircon grains) and there is one spot per rock. Radiation damage was evaluated by either magnetic separation of low-mag. zircons or soaking overnight in HF (Valley et al. 2005). SIMS $\delta^{18}O$ data were analyzed in situ and may include 10's of analyses from a single rock (Valley 2010). SIMS $\delta^{18}O$ analyses are from volumes ~10⁶ times smaller than by laser and are typically less precise (± 0.3 to 0.6% vs. ± 0.1 %, 2SD). Zircons in primitive magmas and in high temperature equilibrium with mantle values of $\delta^{18}O$ fall in the range of 4.7 to 5.9% (5.3 \pm 0.6% VSMOW). Values above this range result from protoliths that underwent low temperature aqueous exchange at the surface of the Earth. Values above 7.5% are rare in the Archean for pristine magmatic zircons, but common for metamorphic and disturbed zircon. Values below 4.7% largely result if protoliths were hydrothermally altered. Hadean and Archean $\delta^{18}O$ (zircon) values above 6% indicate that the surface of the Earth was cool and hospitable to life as early as 4.3 Ga.

Tables

Table 1. Summary of SIMS data for U-Pb ages of zircons JH4.4, JH4.0 and ARG2.5.

Table 2. Oxygen isotope analyses by SIMS of zircons ARG2.5, JH4.0 and JH4.4, and quartz inclusions in JH4.4.

Table 3. Trace element analyses (ppm wt.) by SIMS and APT of zircons ARG2.5, JH4.0 and JH4.4.

Table 4. Ratios of ²⁰⁷Pb/²⁰⁶Pb measured by SIMS and APT in zircons ARG2.5, JH4.0 and JH4.4. Background-corrected atoms of Pb detected and ²⁰⁷Pb/²⁰⁶Pb measured by APT. Pb-rich clusters concentrate Pb, Y and REEs in ARG2.5 and JH4.4 and are defined based on Y concentration, see text.

Appendix 1. Rotating images of Y and Pb.

Table 1.

Spot	grain t area	U (ppm)	Th (ppm)	Th/U	²⁰⁶ Pb*/ ²³⁸ U age (Ma)	1s err	²⁰⁷ Pb*/ ²⁰⁶ Pb age (Ma)	1s err	²⁰⁸ Pb*/ ²³² Th age (Ma)	1s err	% conc.
ARC	G2.5	(ARG0	5-28-2))							
2.	1 core	672	224	0.35	2462	9	2542	5			97
JH4	1.0	(01JH1	3b-8-4))							
8.4.2	2 mantle	e 157	17	0.11	3904	21	4007	22			97
JH4	1.4	(01JH3)	86-69)								
1	core	140	92	0.66	4412	25	4382	5	4445	47	101
2	core	138	95	0.71	4349	24	4365	5	4374	52	100
3	core	93	66	0.74	4391	29	4374	6	4384	61	100
4	rim	61	16	0.27	3436	42	3379	13	3050	147	102
5	rim	119	189	1.64	2798	19	3391	12	492	26	83
6	rim	58	43	0.77	3053	32	3430	16	1206	62	89

References:

(1) Strickland pers. comm 2012

(2) Strickland et al. 2011

(3) Cavosie 2005

(4) Valley et al. 2014

CHECK Th/U RATIOS.

Ref.

1,2

3

4 4 4

4 4 4

Errors are 1σ unless otherwise specified

Table 1. zircon 01JH36-69

 Pit	# rej	204 cts /sec	204 /206	% err	207 /206	% err	232Th /238U	208 /206	% err	Obs 206 /238
1	0	0.05	2E-05	45.5761	0.55052	0.354487	0.677491	0.170223	0.672318	1.801217
2	0	0.17	7E-05	28.944	0.544336	0.354866	0.713997	0.181255	0.823605	1.731785
3	0	0.17	1E-04	9.305653	0.548083	0.422277	0.736175	0.185731	1.026811	1.789186
4	0	0.22	3E-04	25.82477	0.285779	0.757903	0.274594	0.072972	1.753163	1.231894
5	0	0.84	6E-04	14.59094	0.291609	0.572142	1.642605	0.095407	1.42467	1.054184
6	0	0.2	4E-04	26.7339	0.296211	0.89423	0.774956	0.09104	1.884501	1.063717

						208-corr		%
%	248	%	254	%	238	Pb/U:	%	comm
err	/254	err	/238	err	/196	UO/U^2	err	206
2.459425	0.630717	0.573779	5.982562	0.646022	0.139242	0.050281	0.784337	0.030642
2.048017	0.666305	0.39795	5.907652	1.241962	0.13867	0.049327	0.76975	0.105631
1.409377	0.68579	0.47513	5.962546	0.690803	0.092579	0.050019	0.923287	0.151741
0.998544	0.25695	0.753212	5.823295	0.859738	0.062264	0.036177	1.586514	0.436096
0.906524	1.52225	3.114038	6.124901	0.666872	0.116452	0.028074	0.832953	0.968635
1.265033	0.725074	0.798853	5.826945	0.953981	0.058385	0.031171	1.317891	0.576433

01JH36-69

					Corr		ppm	Total
ppm	ppm	232Th	Ln	Ln	206	%	Rad	208Pb
U	Th	/238U	UO/U	Pb/U	/238	err	206Pb	/232Th
139.6273	91.55061	0.677491	1.788849	0.588156	0.982882	0.784337	117.9005	0.246955
137.9025	95.29193	0.713997	1.776248	0.548096	0.96424	0.76975	114.2356	0.244781
92.6305	65.99669	0.736175	1.785498	0.580242	0.977768	0.923287	77.80964	0.246683
61.33471	16.29992	0.274594	1.761866	0.204182	0.707171	1.586514	37.26274	0.187927
118.6004	188.5414	1.642605	1.812363	0.043034	0.548774	0.832953	55.91439	0.031874
57.53695	43.15305	0.774956	1.762493	0.055988	0.609316	1.317891	30.11847	0.071581

	204corr		207corr		208corr		204corr	
	206Pb		206Pb		206Pb		207Pb	
%	/238U	1σ	/238U	1σ	/238U	1σ	/206Pb	1σ
err	Age	err	Age	err	Age	err	Age	err
1.181701	4411.922	25.06272	2702.793	371.8396	4409.775	26.87568	4382.208	5.190522
1.195493	4348.667	24.36597	2689.14	356.9105	4346.91	26.2706	4364.826	5.224623
1.460325	4391.415	29.40734	2705.031	368.2295	4391.961	31.80687	4374.372	6.211608
2.481519	3436.131	42.3704	#NUM!	#VALUE!	3446.851	43.61686	3378.56	12.98989
3.524305	2797.91	19.23233	2427.163	69.54737	3241.58	51.32326	3390.829	12.10021
2.434409	3053.178	32.28366	2712.762	82.77088	3205.343	36.79193	3430.165	15.55682

204corr			%					
208Pb			Dis-	4corr		Total		Total
/232Th	1σ		cor-	208r	%	238	%	207
Age	err		dant	/232	err	/206	err	/206
4444.849	46.66551	100.6781	-0.67349	0.245963	1.049878	1.017416	0.784337	0.55052
4373.945	52.30536	99.62978	0.371593	0.2416	1.19584	1.037086	0.76975	0.544336
4383.523	61.4371	100.3896	-0.3881	0.242189	1.401546	1.022738	0.923287	0.548083
3050.049	147.1001	101.704	-1.67546	0.162882	4.822875	1.414084	1.586514	0.285779
492.3425	25.98203	82.51402	21.19152	0.024658	5.277225	1.822243	0.832953	0.291609
1205.826	62.40264	89.00965	12.34736	0.061474	5.175096	1.641185	1.317891	0.296211

ave 7/6 0.547646 2SD 7/6, n= 0.00623 0.8% 7/6 0.004381

%	238/ 206r	%	207r /206r	%	207r /235	%	206r /238	%
err		err		err		err	1236	err
0.354487	1.017728	0.784463	0.550394	0.354877	74.56638	0.861	0.982581	0.784463
0.354866	1.038182	0.770386	0.543895	0.356874	72.23412	0.849031	0.963222	0.770386
0.422277	1.024292	0.923444	0.547454	0.42451	73.69274	1.016345	0.976284	0.923444
0.757903	1.420278	1.590778	0.282817	0.832935	27.45578	1.795649	0.704088	1.590778
0.572142	1.840067	0.84731	0.285052	0.776601	21.35954	1.149366	0.543459	0.84731
0.89423	1.650701	1.327471	0.292351	1.001374	24.41953	1.662808	0.605803	1.327471

err corr

0.911108

0.907371

0.908593

0.885907

0.737197

0.798331

Table 2.

Sample Analysis spot	Age Ma ¹	Loc. ³	$\delta^{18}O$ VSMOW ⁴	2 SD ⁵	$\delta^{17}O$ VSMOW ⁴	2 SD ⁵	$\Delta^{17}\mathrm{O}$	2 SD ⁵	Ref.
ARG2.5	(ARG0	5-28-2)							
ARG05-28-2	2542	core							1,2
	-	mantle	6.21	0.23					2
	-	mantle	5.38	0.23					2
JH4.0	(01JH1	3b-8.4 (2.5	5M))						
July. 19, 2006									
2.5M 8.4.1	4007	mantle	5.81	0.23					3
2.5M 8.4.2	-	dist. core	4.09	0.23					3
2.5M 8.4.3	4007	mantle	5.95	0.23					3
2.5M 8.4.4	4007	mantle	5.84	0.23					3
	avg. Zr	c rim (n=3)	5.87	0.15					
Dec. 21, 2006									
01JH13b_2.5M	1 8-4	mantle	6.01	0.15	3.04	0.28	-0.09	0.26	4
JH4.4	(01JH-	36-69 (5M))						
July. 28, 2006									
5M 69.1	4374	core	4.73	0.34					5
5M 69.2	4374	core	4.47	0.34					5
5M 69.3	4374	core	4.94	0.34					5
5M 69.4	4374	core	4.78	0.34					5
5M 69.5	~3400	rim	5.73	0.34					5
5M 69.6	~3400	rim	5.36	0.34					5
5M 69.7	~3400	rim	5.87	0.34					5
5M 69.8	~3400	rim	5.47	0.34					5
5M 69.9	-	dist.	3.54	0.34					5
5M 69.10	4374	core	5.00	0.34					5
5M 69.11	4374	core	4.81	0.34					5
5M 69.Q1	-	qt.incl.	12.49	0.28					6
5M 69.Q2	-	qt.incl.	12.43	0.28					6
5M 69.Q3	-	qt.incl.	12.84	0.28					6
	avg. Zr	c core (n=6	4.79	0.37					
	avg. Zr	c rim (n=4)	5.60	0.47					
	avg. Qt	(n=3)	12.59	0.44					
Dec. 21, 2006									
01ЈН36 69-1	4374	core	4.88	0.25	2.59	0.13	0.05	0.21	4,5
01ЈН36 69-2	4374	core	4.84	0.25	2.56	0.13	0.05	0.21	4,5
01ЈН36 69-3	4374	core	4.66	0.25	2.53	0.13	0.10	0.21	4,5
01JH36 69-4	-	dist.	3.56	0.25	2.03	0.13	0.18	0.21	4,5

 $^{^{1}}$ 207 Pb/ 206 Pb age. Ma = Mega annum

 $^{^{2}}$ 2SD = 2 standard deviations.

³Loc. = location within zircon: core, rim, mantle, incl. = mineral inclusion, dist. = disturbed zi domain.

Table 2.

Sample	Age	T 3	$\delta^{18}O$	2 CD5	$\delta^{17}O$	2 CD5	1170	2 GD5	Ref.
Analysis spot	Ma^1	Loc.	δ ¹ °O VSMOW ⁴	2 SD	VSMOW ⁴	2 SD	Δ.Ο	2 SD	6

⁴Corrected value, VSMOW.

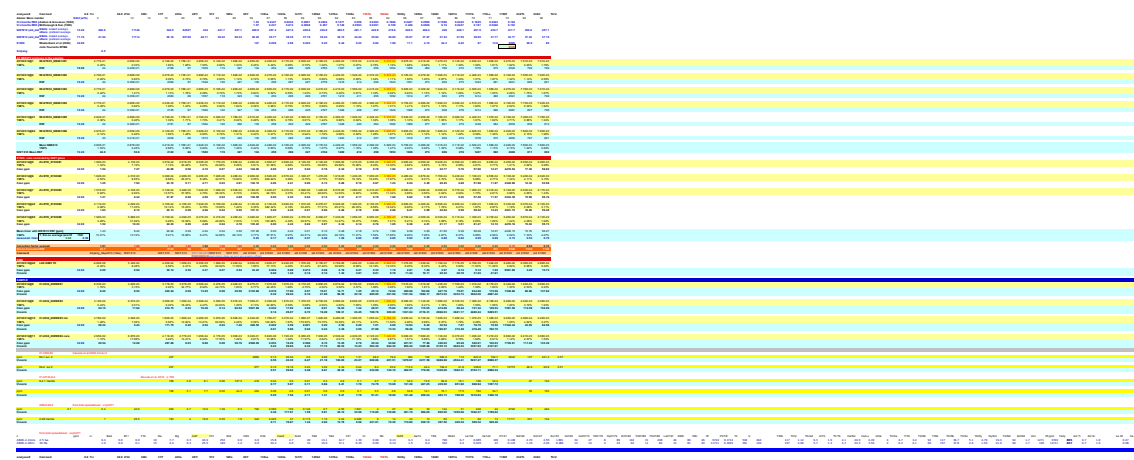
 5 The 2SD of an individual analysis is based on the spot-to-spot reproducibility of two 'bracke of standard analyses. (8 spots). A 'bracketing set' consists of four analyses of KIM-5 (UWQ-1 for Qz), before andafter every10-12 sample analyses. The 2SD listed with the sar averages is based on measured δ if at least three measurements were made.

⁶References:

- (1) Strickland, pers. comm. 2011
- (2) Strickland et al. 2011b
- (3) Cavosie et al. 2005; Ushikubo et al. 2008
- (4) Valley et al. 2007
- (5) Valley et al. 2014a
- (6) this study

ting sets'

mple



| Second Second



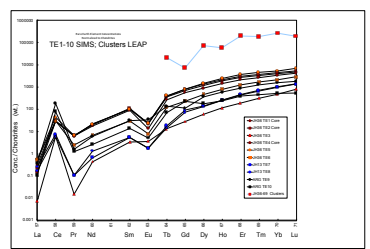


Table 3.

Zircon	JH4.4 ³	JH4.4 ³	JH4.4 ³	JH4.4 ³	JH4.4 ⁴	JH4.4 ⁴	JH4.0 ²	JH4.0 ²	ARG2.5	ARG2 5	.IH4 4 ³
Spot	TE1	TE2	TE3	TE4			TE7	TE8		TE10	APT
- 1	Core	Core	Rim			3urface2	Mantle	Mantle			Clusters
Li	6.2		29.3	20.5			56.2	45.2		1	6
Al	8.5	11.6	5.4	12.1					40.9	25.5	200
Р	222	214	112	288	407	237	166	196	252	183	1600
Ca	0.1	0.2	0.4	6.0			3.6	3.1	2.7	4	30
Ti	13.2	18.4	2.5	10.0			6.1	7.7	12.9	16.8	
V	0.1	0.1	0.02	0.1			0.06	0.02	1.4	0.4	
Fe	45.6	62.5	7.4	39.8			107.3	44.3	6.3	1.5	
Υ	3133	3528	226	2508	2869	977	418	454	790	342	105000
La	0.08	0.03	0.002	0.05	0.13	0.12	0.04	0.06	0.09	0.03	
Ce	17.8	17.8	3.6	18.3	26.5	18.2	3.6	4.6	109.0	47.0	
Pr	0.6	0.6	0.001	0.6	0.6	0.2	0.01	0.01	0.1	0.1	
Nd	10.0	8.9	0.2	8.1	9.7	3.0	0.3	0.6	2.7	1.2	
Sm	14.7		0.5	13.3	14.8	4.3	8.0	8.0	4.55	2.0	
Eu	1.2	1.3	0.2	0.8	1.3	0.4	0.1	0.1	1.9	0.3	
Gd	72.0	75.6	2.7	52.6	79.9	23.9	3	3.6	27	14	4300
Tb	25.1	28.5	1.0	20.3	29.2	8.4	2.7	3.3	4	8	250
Dy	290.7	327.4	14.6	221.5	364	113.3	32.3	34.8	89	43	18000
Но	102.9	115.6	6.2	77.9	132		13.5	14.1	32	13	3200
Er	427.8	474.9	30.5	340.0			69.6	74.1	144	62	31000
Tm	79.9	89.4	7.7	65.3	112		16.1	17.5	31	11	5000
Yb	634.7	721.3	76.7	540.6			156	164	248	82	43000
Lu	115.6	129.5	19.5	102.0	169.7	71.1	33.4	34.1	44	13	5700
Hf	7350	7282	11544	7730	9642				9722	11711	4600
Th	97	113	23	111	137	48	27	39	518	301	
U	138	152	83	133	241	94	193	163	464	104	
Th/U	0.70	0.74	0.28	0.83	0.57	0.51	0.14	0.24	1.12	2.89	
ΣREE	1793	2007	163	1461	2373	865	331	352	737	297	110450